PHYSICAL REVIEW A VOLUME 39, NUMBER 2 JANUARY 15, 1989

Multimode instability in optical bistability

B. Ségard and B. Macke
Laboratoire de Spectroscopie Hertzienne, Université de Lille, F-59655 Villeneuve d'Ascq Cédex, France

L. A. Lugiato
Dipartimento di Fisica del Politecnico, Corso Duca degli, Abruzzi 24, 10129 Torino, Italy

F. Prati and M. Brambilla
Dipartimento di Fisica dell Universitá, Via Celoria 16, 20133 Milano, Italy

(Received 20 June 1988)

We compare theoretical predictions and experimental data for the multimode instability of optical bistability, which arises from the coherent dynamics of a system of two-level molecules contained in an optical cavity and driven by an external stationary laser field. Considerable insight into this phenomenon is provided by two "rules of thumb" that govern the behavior of the self-pulsing frequency, and establish its relation with the Rabi frequency of the intracavity field. We describe in detail the experimental apparatus and the main features of the experimental findings. The theoretical results are based on the Maxwell-Bloch equations for a ring cavity in the plane-wave approximation. Despite the crudeness of this model, the numerical data display a satisfactory qualitative agreement with the experimental results. Additional period-doubling and chaotic phenomena, predicted by the theory and not observed in the experiment, are presumably washed out by the longitudinal and radial variation of the electric field in the cavity.

I. INTRODUCTION

After the discovery of the self-pulsing regimes in homogeneously broadened masers and lasers,[1-5] the field of optical instabilities has been much investigated under the joint impulses arising from the investigation of instabilities in the optical bistability (OB),[6,7] the experimental observation of self-pulsations in inhomogeneously broadened lasers,[8] and the discovery of optical chaos.[9,10] General references on the subject of optical instabilities are found in Refs. 11–15.

From a fundamental viewpoint, most relevant are the instabilities which arise in systems with constant parameters, in absence of any modulation or addition of any feedback different from that which arises intrinsically from the optical cavity. Classic are the instabilities that emerge in the framework of the set of the Maxwell-Bloch equations for a ring cavity and a homogeneously broadened system of two-level atoms. Due to its relative simplicity and to the fact that it includes the fundamental elements of the atom-field interaction, this model represents the paradigm of nonlinear, dissipative dynamical system in the framework of quantum optics.

It is customary to distinguish single-mode (SM) and multimode (MM) instabilities. This procedure is based on the notion of the resonant mode which, in the case of externally driven systems, is defined as the longitudinal cavity mode nearest to the frequency of the input field. In SM instabilities the resonant mode itself becomes unstable, whereas in MM instabilities one or more longitudinal side modes of the resonant mode are destabilized.

In order to ensure single-mode operation, it is sufficient to satisfy two conditions: (1) the reflectivity coefficient R of the cavity mirrors must be close to unity, to guarantee that the longitudinal modes are narrow and well separated from one another; (2) the atomic linewidth must be much smaller than the frequency spacing of the cavity modes, to exclude that the atom-field interaction induces an instability in a side mode of the resonant mode. Condition (1) implies that the absorption coefficient αl must be small to ensure that the bistability parameter $C=\alpha l/2(1-R)$ remains finite in the limit $R\rightarrow 1$. Furthermore, in order to have any transmission at all, the frequency separation between the driving field and the resonant mode must be on the order of or smaller than the cavity linewidth, which becomes small for $R\rightarrow 1$. Finally, in condition (2) one must take into account the power broadening in the atomic line.

On the other hand, a MM instability can arise only if the power-broadened atomic linewidth is on the order or larger than the free spectral range; this condition requires a large atomic linewidth and/or a long cavity, and is not satisfied in the standard homogeneously broadened all-optical systems which meet the conditions for the two-level-system description. This feature makes it very difficult to observe experimentally MM instabilities which arise from the interplay of different longitudinal modes, unless one uses a hybrid system which includes a delay line.[16]

Single-mode and multimode instabilities are linked by precise correspondence principles demonstrated in Ref. 17, which provides a fundamental justification of the so-called "weak-sideband approach," that is often used in the interpretation and discussion of optical instabilities.[18-23] This approach ascribes the rise of the instability to the gain experienced by the various modes, which work as weak probe fields in the presence of the strong cavity field. As is well known, a probe field can undergo amplification even in a passive medium without population inversion.[24-26] The analysis of Ref. 17 shows that the same gain function determines both single and multimode instabilities, and the rise of a SM or a MM instability depends only on which cavity mode lies in the frequency regions characterized by the presence of gain. The two kinds of instabilities remain, however, quite different from the operational viewpoint of an experimental observation: in the SM case, one must fulfil the conditions for single-mode behavior, whereas in the case of MM instabilities one must push under the atomic line at least one cavity side mode of the resonant mode.

The single-mode instability of OB was predicted,[27,28] and experimentally observed[29,30] using a short (5-cm) ring cavity crossed at right angles by ten atomic beams of sodium, in a configuration which satisfies the conditions for single-mode operation. The experimental data are in satisfactory agreement[31] with the predictions of a model which assumes that the internal field retains the same Gaussian radial profile of the input field.[28]

The multimode instability of optical bistability, predicted in Refs. 6 (purely absorptive case) and 32 (mixed absorptive plus dispersive OB) and analyzed in Refs. 33–35 has been recently observed experimentally using a microwave Fabry-Pérot cavity filled with $HC^{15}N$.[36,37] The large cavity length (182 m) and power broadening ($\cong$ factor of 40) allow a side mode of the resonant mode below the atomic line.

We note that both the SM instability observed in Ref. 29 and the MM instability observed in Ref. 36 arise from the coherent dynamics of the atom-field interaction, and therefore require a full set of Maxwell-Bloch equations for their description. This is different from the Ikeda instabilities,[10,16] which arise basically from delay mechanisms and can be described in the rate equation approximation.

Furthermore, the SM and MM instabilities of OB are the passive counterpart of the classic instabilities in homogeneously broadened lasers;[1-5] in the laser case the experimental observation of these instabilities[38-40] is still a focus of discussion.

The aim of this paper is to provide a detailed comparison between theoretical predictions and experimental data for the MM instability of OB; in this sense, this work is complementary to Ref. 31 which carries out the same program for the SM instability of OB. In the case of this paper, the comparison is rather crude because our numerical simulation is based on the Maxwell-Bloch equations for a ring cavity and in the plane-wave approximation, whereas in the experiment the cavity is of Fabry-Pérot type and the radial profile of the electric field corresponds to the Bessel function J_1. Nonetheless, we find a satisfactory and systematic correlation between our numerical results and the experimental data.

A key role is played by the two "rules of thumb" which characterize this instability,[41] in the sense that they establish the behavior of the frequency of the spontaneous oscillations in the output intensity, and its relation with the Rabi frequency of the intracavity field. These rules provide physical insight, allow describing in an organized and unified way the theoretical and experimental results, and identifying without ambiguity the experimentally observed instability as that predicted a long time ago in Ref. 6.

In Sec. II we review the set of Maxwell-Bloch equations that we use in our calculations, and formulate precisely the two rules of thumb. Section III is devoted to the detailed description of the experimental apparatus and results. In Sec. IV we illustrate the numerical results and compare them with the experimental data.

II. DYNAMICAL EQUATIONS AND RULES OF THUMB FOR THE MULTIMODE INSTABILITY

Figure 1 illustrates (a) a Fabry-Pérot of length l and (b) an "equivalent" ring cavity of length $2l$; we will consider the latter configuration in our numerical calculations. We assume that mirrors 2 and 3 in Fig. 1(b) are ideal reflectors, while mirrors 1 and 4 have reflectivity coefficient R. In order to match the experimental situation, we allow in general the transmissivity coefficient T of mirrors 1 and 4 to be smaller than $1-R$. The input field E_i is stationary, coherent, and has a frequency ν_0. The cavity is filled with a large number of identical two-level molecules of transition frequency ν_m. We indicate by $\gamma_\perp$ and $\gamma_\parallel$ the relaxation rates of the molecule polarization and population difference, respectively; $\gamma_\perp$ coincides with the linewidth of this homogeneously broadened system.

In the dipole, rotating-wave and plane-wave approximations the dynamics of the system molecules plus field in the ring cavity is governed by the Maxwell-Bloch equations

$$\frac{\partial F}{\partial z}+\frac{1}{c}\frac{\partial F}{\partial t}=-\frac{\alpha}{2}P\,, \tag{2.1a}$$

$$\frac{\partial P}{\partial t}=\gamma_\perp[FD-(1+i\Delta)P]\,, \tag{2.1b}$$

$$\frac{\partial D}{\partial t}=-\gamma_\parallel[\tfrac{1}{2}(F^*P+FP^*)+D-1]\,, \tag{2.1c}$$

where F is the normalized slowly varying envelope of the

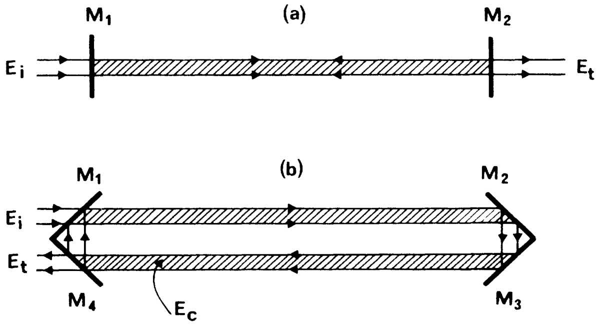

FIG. 1. (a) Fabry-Pérot cavity. M_1 and M_2 are lossless semitransparent mirrors of reflectivity R. (b) Equivalent ring cavity (ERC). M_2 and M_3 are totally reflecting mirrors; M_1 and M_4 have reflectivity coefficient R and transmissivity coefficient T. In presence of losses, $T+R<1$.

electric field, defined by

$$F(z,t)=2\pi\frac{\nu_r(z,t)}{(\gamma_\perp\gamma_\parallel)^{1/2}}\ , \tag{2.2}$$

where $\nu_r(z,t)$ is the Rabi frequency (in Hz) of the intracavity field; D and P are the normalized population difference and the normalized slowly varying envelope of the molecular polarization, respectively.[42] The parameter α is the unsaturated absorption coefficient per unit length on resonance for the intensity; Δ is the molecular detuning parameter given by

$$\Delta=2\pi\frac{\nu_m-\nu_0}{\gamma_\perp}\ . \tag{2.3}$$

The ring cavity configuration imposes the boundary condition[42]

$$F(0,t)=Ty+Re^{-i\delta_0}F(2l,t)\ , \tag{2.4}$$

where the normalized input field y is given by

$$y=2\pi\frac{\nu_{ri}}{(\gamma_\perp\gamma_\parallel T)^{1/2}}\ , \tag{2.5}$$

with ν_{ri} the Rabi frequency of the injected field, and the cavity detuning parameter δ_0 defined by

$$\delta_0=2\pi\frac{\nu_p-\nu_0}{c/2l}\ . \tag{2.6}$$

In Eq. (2.6) ν_p can be any cavity frequency. Usually ν_p is chosen as the mode which is nearest to the frequency ν_0 of the input field (resonant mode); in our case, instead, it is convenient to select ν_p as the cavity frequency nearest to the molecular frequency ν_m (Fig. 2). The reason for this choice is to avoid discontinuous jumps of δ_0 when the input frequency ν_0 is swept between two adjacent cavity modes.

The stationary solutions are obtained by dropping the time derivatives in Eq. (2.1). Introducing the parameter

$$\eta=\frac{|F(0)|}{|F(2l)|} \tag{2.7}$$

and the normalized transmitted field

$$x(t)=|F(2l,t)|=\frac{2\pi\nu_{rt}(t)}{(\gamma_\perp\gamma_\parallel T)^{1/2}}\ , \tag{2.8}$$

where ν_{rt} is the Rabi frequency of the transmitted field, the stationary-state solutions are governed by the parametric equations.[42]

$$x^2=2[\alpha l-(1+\Delta^2)\ln\eta]/(\eta^2-1)\ , \tag{2.9a}$$

$$y^2=x^2(\eta)\{(\eta-R)^2+4R\eta\sin^2[\tfrac{1}{2}(\Delta\ln\eta-\delta_0)]\}/T^2\ , \tag{2.9b}$$

where $x^2(\eta)$ in Eq. (2.9b) is given by Eq. (2.9a). A general linear-stability analysis of these stationary solutions is given in Ref. 43. The negative-slope portions of the steady-state curve of transmitted intensity as a function of input intensity are always unstable.

While in Refs. 6 and 34 one considers arbitrary parameters, the MM instability predicted in Ref. 6 was mainly analyzed in the so-called "mean-field" or "uniform-field" limit defined by the conditions

$$\alpha l \ll 1,\quad 1-R\ll 1,\quad \delta_0 \ll 1\ , \tag{2.10a}$$

with

$$C=\frac{\alpha l}{2(1-R)}\ \text{and}\ \theta=\frac{\delta_0}{1-R}\ \text{arbitrary}\ ; \tag{2.10b}$$

in this case ν_p in Eq. (2.6) is defined as the cavity frequency nearest to the input frequency ν_0. In this limit the steady-state equation reduces to

$$y=x\frac{1-R}{T}\left[\left(1+\frac{2C}{1+\Delta^2+x^2}\right)^2+\left(\theta-\frac{2C\Delta}{1+\Delta^2+x^2}\right)^2\right]^{1/2}\ , \tag{2.11}$$

and the MM instability is characterized by arising in conditions of quasiresonance between the Rabi frequency ν_r of the intracavity field and the free spectral range $c/2l$. The frequency of the spontaneous oscillations in the output intensity, originated by the instability, is also near to the free spectral range.

The experimental conditions, in which oscillations are observed in Refs. 36 and 37 do not fulfill the mean-field condition (2.10a). The reflectivity coefficient R is not close to unity, and the absorption parameter αl is much larger than unity. The latter feature is, in fact, much less dramatic than expected because the oscillations arise in the upper branch of the hysteresis cycle of output versus input power, under conditions in which the saturated absorption parameter $\alpha l/(1+\Delta^2+x^2)$ is smaller than unity.[44] The condition $\delta_0 \ll 1$ is, however, badly violated in Refs. 36 and 37. Hence it is necessary to generalize the usual picture of the MM instability to the parametric domains well out of the mean-field limit.

A straightforward procedure to achieve this goal is offered by the "weak-sideband" or "gain-feedback" approach to optical instabilities,[18–23] which in the case of multimode instabilities can be rigorously justified on the basis of the linear stability analysis.[17,43] This approach

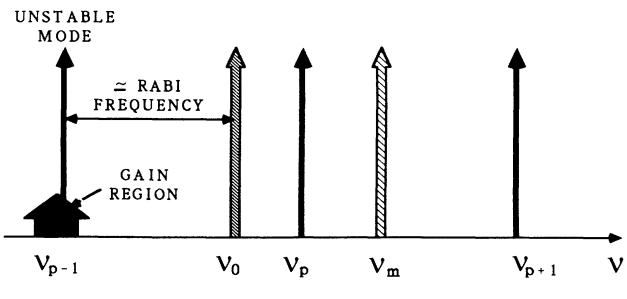

FIG. 2. Schematic representation of the frequencies in play: ν_p and $\nu_{p\pm1}$ are cavity frequencies, ν_0 is the input field frequency, and ν_m is the transition frequency of the two-level molecules.

starts from the fact that when a weak probe beam interacts with a passive two-level medium saturated by a strong field, there are frequency regions in which the probe experiences gain instead of absorption; in this way, one can obtain gain without any population inversion.[24–26] The concluding section of Ref. 45 proposed to enclose the medium in an optical cavity resonant at a frequency for which the medium is amplifying, in order to realize an oscillator. This result was achieved recently, using cavities which provide feedback only to the probe beam, and obtaining laser action at the probe frequency.[46,47]

In the case of optical instabilities of the type we are considering here, the cavity provides feedback also to the strong field, i.e., the input field of the optically bistable system. The cavity modes act as probe fields; if some of them lie in frequency regions where there is gain, and if this gain is larger than the losses of the modes, an initial random fluctuation provides the impetus for these modes to grow, and the stationary state is destabilized. When, as in the case of the instabilities observed in Refs. 29 and 36, only one cavity mode becomes unstable the frequency of the spontaneous oscillations of the output intensity is the beat note between the frequency of the unstable mode and the input frequency.

Unfortunately, in this argument there is one element that cannot be determined in a straightforward way, i.e., the frequency of the cavity mode when it interacts with the nonlinear medium. In fact, dispersion displaces the cavity frequencies with respect to their empty cavity values. In this paper, we will follow two options: (1) to use the empty-cavity value $c/2l$ for the mode spacing or (2) to use the value of the mode spacing obtained from the stationary curve by sweeping the input frequency between two adjacent modes of the filled cavity; this procedure gives a value of the mode spacing which depends on the input intensity and is larger than $c/2l$. Indicating by ν_{th} the value of the oscillation frequency predicted by the theory, and by ν_s the frequency of the unstable mode, we will indicate the prescription

$$\nu_{\text{th}}=|\nu_s-\nu_0| \tag{2.12}$$

as the "first rule of thumb" of the MM instability. The two different values for ν_{th}, obtained by following prescriptions (1) and (2), will be indicated by $\nu_{\text{th}}^{(1)}$ and $\nu_{\text{th}}^{(2)}$, respectively. We note that in the mean-field limit, in which the cavity detuning parameter δ_0 is small and the effect of dispersion on the cavity frequencies is negligible, Eq. (2.12) reduces to the well-known result that the oscillation frequency coincides with the free spectral range.

In the experiment[29] the oscillation frequency which arises from the single-mode instability is close to the difference between the empty-cavity frequency of the resonant mode and the input frequency, and is therefore essentially proportional to the cavity detuning parameter; the rule (2.12) describes quite well the behavior of the oscillation frequency.

In the case of the MM instability observed in Ref. 36, ν_s coincides with ν_{p-1} or ν_{p+1} (Fig. 2); the prescription (2.12) will be compared with experimental and numerical data in the following sections. Our analysis will show also that there is a systematic correlation between the oscillation frequency and the Rabi frequency of the intracavity field. The second rule of thumb (Fig. 2)

$$\text{Oscillation frequency} = \text{Rabi frequency of the internal cavity field} \tag{2.13}$$

was already mentioned in connection with the mean-field limit, but remains valid in general. Out of the mean-field limit the Rabi frequency varies along the medium, but this is not a difficulty because the prescription (2.13) pretends to give only an estimate of the oscillation frequency; for the sake of accuracy, we will consider the value of the Rabi frequency just before the output mirror. Here, again, we meet different options that concern the precise definition of the Rabi frequency to be considered in the rule (2.13): we indicate by $\nu_r^{(1)}$ and $\nu_r^{(3)}=\{(\nu_r^{(1)})^2+[(\gamma_\perp/2\pi)\Delta]^2\}^{1/2}$ the Rabi frequency and the generalized Rabi frequency, respectively, obtained from the value of the intracavity field in the unstable stationary solution; we indicate by $\nu_r^{(2)}$ and $\nu_r^{(4)}=\{(\nu_r^{(2)})^2+[(\gamma_\perp/2\pi)\Delta]^2\}^{1/2}$ the Rabi frequency and the generalized Rabi frequency, respectively, obtained from the r.m.s. value of the intracavity field in the oscillations which arise from the instability of the stationary solution. Of course, in the experiment only $\nu_r^{(2)}$ and $\nu_r^{(4)}$ are available.

The correlation with the Rabi frequency strongly suggests that this instability arises from what is usually called the Raman gain;[47,48] it must be kept in mind, however, that the exact theoretical expression of the gain which governs the instability is provided by the linear stability analysis and, in the plane-wave approximation is given by the expressions reported in Ref. 17 for the mean-field limit and in Ref. 43 for the general case.

We expect that the same rules of thumb hold for the laser instability in Ref. 4 and 5, when it is generalized out of the mean-field limit; in this case, ν_0 in Eq. (2.12) should be understood as the oscillation frequency of the field in the stationary state of the laser. In more general terms, one can observe that, after experimental results as the ones obtained in Refs. 46 and 47, the distinction between active and passive systems becomes much weaker. This fact does not eliminate, however, the existence of significant differences between instabilities in active and passive systems; for example, the MM laser instability of Refs. 4 and 5 disappears in the rate equations approximation, whereas in the case of OB one obtains a MM instability even from the rate equation in the mean-field limit.[49]

III. EXPERIMENTS

Our experiments have been made at a millimetric wavelength ($\lambda \cong 3.5$ mm) in a Fabry-Pérot cavity containing a molecular gas at low pressure.[36] The use of millimetric waves, unconventional in the studies of nonlinear optics, has the following advantages.

(1) The amplitude noise of the available source (klystrons) is much lower than that of most lasers.

(2) Some molecules have in this domain well-isolated rotational lines, heavily absorbing in linear regime but saturable by reasonable fields ($\cong 0.1$ V/cm).

(3) The Doppler effect is quite moderate ($\cong 100$ kHz) and it is then possible to approximate the ideal homogeneously broadened two-level medium with a bulk gas.

(4) The relaxation times, fixed by the molecular collisions, are long, in inverse ratio to the gas pressure p ($T_1 \cong T_2 \cong 7$ μs at $p=1$ mTorr in our experiment).

(5) It is possible to guide the electromagnetic beam in a well-defined mode with very low losses, avoiding the problems related to self-focusing and self-defocusing effects. This enables one to develop very long cavities (182 m in our experiment) and, since the frequency of the multimode instabilities is expected to be of the order of the free spectral range, to observe these instabilities in real shape, without any particular treatment (filtering, averaging, etc., . . .) required at higher frequencies.

We present in Sec. III A the physical system under investigation, in III B the experimental arrangement, and in III C our observations of self-pulsing.

A. Physical system

The requirement of a heavily absorbing and easily saturable two-level transition naturally leads to considering the rotational line $(J=0,M=0)\rightarrow(J=1,M=0)$ of a strongly polar molecule, as light as possible, since the absorption coefficient α_∞ (collisional limit) increases roughly as the cube of the line frequency in the microwave domain.[50] We have restricted our field of investigation to the frequencies lower than 100 GHz ($\lambda=3$ mm) where low-noise and sufficiently powerful klystrons of reasonable cost are available. The best molecule then appears to be hydrocyanic acid (HCN). Unfortunately the strong electric quadrupolar moment of ^{14}N entails an important splitting of the lines of the most abundant isotopomer HC^{14}N (3 MHz for the 0-1 line).[51] Our interest has then be brought to the isotopomer HC^{15}N which presents only a very narrow hyperfine structure, resulting mainly from the coupling of the spins $\frac{1}{2}$ of ^{15}N and H with the rotation. The corresponding hyperfine Hamiltonian (in frequency units) reads

$$H_{\mathrm{hf}}=C_{\mathrm{N}}\mathbf{J}\cdot\mathbf{I}_{\mathrm{N}}+C_{\mathrm{H}}\mathbf{J}\cdot\mathbf{I}_{\mathrm{H}} , \tag{3.1}$$

with $C_{\mathrm{N}}=-6.92$ kHz, $C_{\mathrm{H}}=-4.20$ kHz,[52] and where $\mathbf{J}$, $\mathbf{I}_{\mathrm{N}}$, and $\mathbf{I}_{\mathrm{H}}$ are, respectively, the rotational angular momentum, the spin of ^{15}N, and the spin of H. Neglecting the hyperfine effects, the 0-1 line of HC^{15}N is characterized by the transition frequency $\nu_m=86.054\,961$ GHz (Ref. 53) and a single Rabi frequency[54] $\nu_r=\mu E/h\sqrt{3}$ ($\mu=2.986$ D, the dipole moment of HC^{15}N,[55] E is the amplitude of the microwave field). The line is in fact split by the spin-rotation coupling in four components (Fig. 3) which are not resolved in conventional linear spectroscopy. We checked the influence of this structure on the nonlinear response of the system. For this purpose, the Bloch equations in the rotating-wave approximation[54] were solved by standard computational procedures in the 16-dimension space subtended by the rotational states $J=0$ and $J=1$, neglecting any homogeneous and inhomogeneous relaxation. Figure 4 gives the result obtained in the case of a stepwise incident field, resonant with the transition frequency ν_m in the absence of hyperfine effects. As expected, a single Rabi frequency, equal to ν_r previously defined, is present in the oscillations as soon as ν_r significantly exceeds the hyperfine splitting. This condition is always fulfilled in our experiments. The hyperfine effects may then be ignored and the HC^{15}N molecules may thus be considered as ideal two-level systems.[54,56]

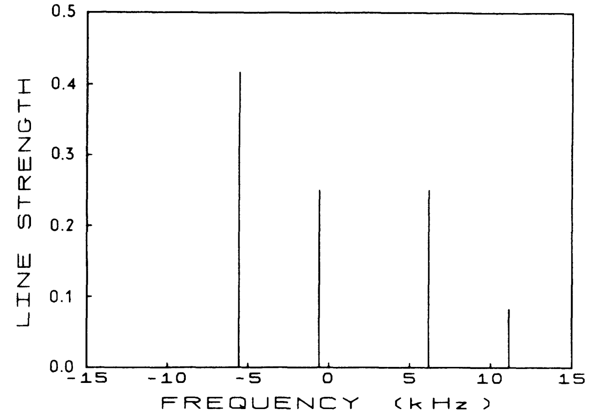

FIG. 3. Hyperfine structure of the $J=0\rightarrow J=1$ line of HC^{15}N. The frequency 0 is that of the line when the hyperfine effects are neglected and the vertical unit is the corresponding intensity of the line.

As indicated before, the relaxation mechanism of the rotational transitions is essentially collisional and may generally be characterized by an unique rate ($\gamma_\parallel \cong \gamma_\perp = \gamma$), proportional to the gas pressure. For the 0-1 line of HC^{15}N, the measured pressure self-broadening coefficient is $\gamma/2\pi=22.75$ kHz/mTorr,[57] leading to relaxation times $T_1 \cong T_2 \cong 0.7$ μs at $p=10$ mTorr. When the collisional broadening prevails on the power broadening (ν_r) and the Doppler broadening (collisional limit), the dependence of the power absorption coefficient α on the molecular detuning $\delta=\nu_m-\nu_0$ (ν_0 source frequency) is Lorentzian. Its value α_∞ on resonance does not depend on the gas pressure and may be considered as a specific attribute of the line considered.[58] For the 0-1 line of our homemade HC^{15}N, α_∞ was about 1 m^{-1}; slightly below its theoretical value, due to the presence of impurities (see Sec. III B). For the pressures used in the experiments ($p<1.5$ mTorr), the Doppler broadening, though moderate [100 kHz half width at half maximum (HWHM)], prevails on the collisional broadening. The line shape $\alpha(\delta)$ in linear spectroscopy is then a Voigt profile[59] and the absorption coefficient on resonance reads

$$\alpha(0)=\alpha_\infty\sqrt{\pi}\xi\exp(\xi^2)[1-\mathrm{erf}(\xi)] , \tag{3.2}$$

where erf(ξ) is the error function and $\xi=\gamma/kv_0$ (k is the wave number, and v_0 the most probable molecular velocity). For $p=1$ mTorr, we get $\alpha(0)\cong 0.27\alpha_\infty$. In fact, the important quantity is obviously the gas power transmission $\exp[-\alpha(\delta)l]$ where l is the gas thickness. In our experiments, $\alpha(0)l \gg 1$ ($l=182$ m) and only the far wings of the Voigt profile contribute to the transmission. It is well known that these far wings are Lorentzian and we checked that the actual transmission does

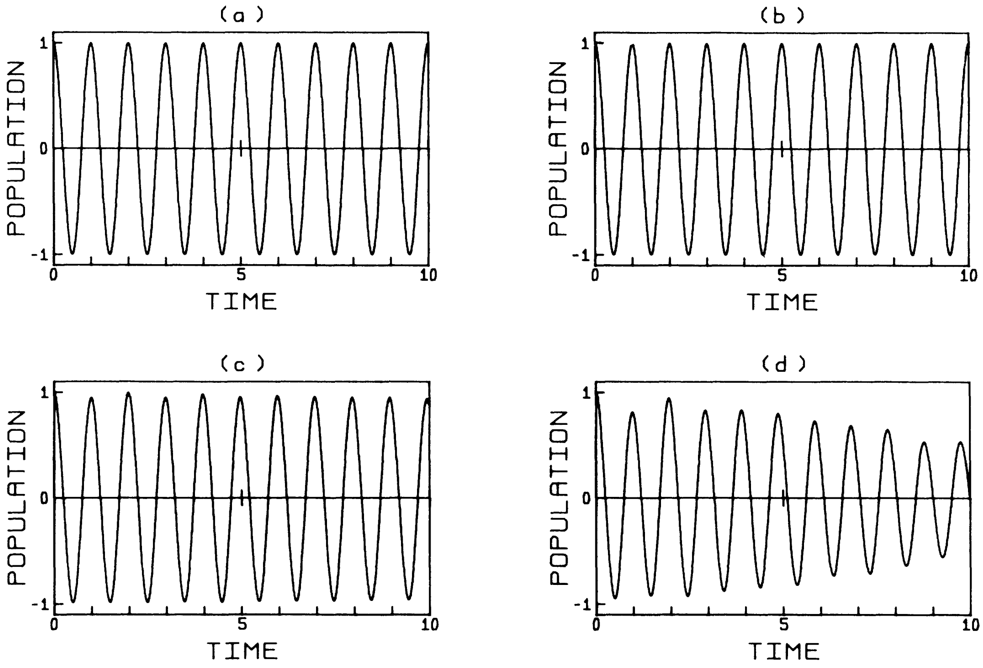

FIG. 4. Rabi oscillations in the presence of hyperfine structure for $\nu_r =$ (a) ∞, (b) 500 kHz, (c) 100 kHz, and (d) 50 kHz. The relative difference of population between the $J=0$ and $J=1$ levels is plotted vs time in $1/\nu_r$ units.

not significantly depart from the transmission $\exp[-\alpha_\infty l/(1+\delta^2/\gamma^2)]$ in the absence of Doppler effect [see Fig. 5(a)]. The same situation occurs (whatever the medium thickness) in the nonlinear regime when the Rabi frequency ν_r (power broadening) prevails over the Doppler broadening, a condition generally fulfilled at the power levels where self-pulsing is observed [see Fig. 5(b)]. The absorption coefficient on resonance reduces then to $\alpha_\infty/(1+\nu_r^2/\gamma^2)$ which may be several orders of magnitude below α_∞. Note, however, that the Doppler effect may affect the response of the strongly driven medium to a probe field, decreasing, for instance, the induced probe gain[45] and then the amplitude of the possible instabilities.

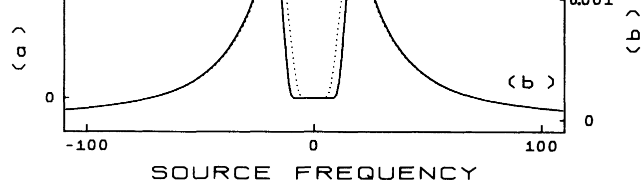

FIG. 5. (a) Power transmission of a 182-m-long sample of $HC^{15}N$ in the absence of saturation. (b) Relative absorption α/α_∞ when the power broadening (Rabi frequency $\nu_r=400$ kHz) prevails on the Doppler width (100 kHz HWHM). These quantities are plotted vs the source detuning $\nu_0-\nu_m$ referred to the collisional broadening, for a pressure of 1 mTorr. The solid curves are exact whereas the dotted lines are obtained when the Doppler effect is disregarded.

The observation of multimode instabilities in a passive cavity containing a two-level medium requires that the Rabi frequency may be brought to a value of the order of the free spectral range (FSR) of the empty cavity[6] (frequency difference $\nu_p-\nu_{p-1}$ between two successive longitudinal modes). This condition is obviously easier to fulfill in a long cavity and, moreover, this facilitates the observation of the self-pulsing, the frequency of which is expected to be comparable to the FSR. We used a Fabry-Pérot cavity of length $l=182$ m [FSR $\nu_p-\nu_{p-1}\cong 830$ kHz (Ref. 60)] consisting of a waveguide cell, initially designed for propagation studies,[61] closed by two identical mesh mirrors of negligible losses (power reflection coefficient $R_0=0.95$, transmission $T_0\cong 1-R_0=0.05$). The waveguide is an oversized helix waveguide (inner diameter $\phi=60\pm0.02$ mm), developed a long time ago for telecommunication applications.[62] The helix structure acts as a mode filter, allowing only the propogation of TE_{0n} modes, such that the components of the electric field in cylindrical coordinates r, θ, and z ($0z$ axis of the helix) read

$$E_r=E_z=0\ , \tag{3.3}$$

$$E_\theta=E_0 J_1(j_{1n}r/a)\cos(\omega t-k_n z)\ , \tag{3.4}$$

where $J_1(x)$ is the first-order Bessel function, j_{1n} its nth zero, and a is the helix radius. Let us notice that this field distribution is that of the so-called parallel beams,[63] recently revisited under the name of diffraction-free beams,[64] and may be seen as resulting from the superposition of an infinity of plane waves, the wave vectors **k** of which are uniformly distributed on a cone of axis Oz, each of them having its electric field linearly polarized perpendicularly to **k** and Oz. Indeed the total electric field fulfills (3.3) and E_θ reads

$$E_\theta = E_0 J_1(k_0 r \sin\bar{\alpha})\cos(\omega t - k_0 z \cos\bar{\alpha}) , \tag{3.5}$$

where $\bar{\alpha}$ is the half-angle of the cone and k_0 is the free-space wave number. The tangential field must cancel on the helix and this obviously fixes the values $\bar{\alpha}_n$ allowed for $\bar{\alpha}$ and the corresponding wave number k_n:

$$k_0 a \sin\bar{\alpha}_n = j_{1n}, \quad k_n = k_0 \cos\bar{\alpha}_n . \tag{3.6}$$

In our oversized waveguide ($a = 30$ mm, $\lambda_0 = 3.5$ mm), 16 modes are allowed to propagate (for $n > 16$, $\sin\bar{\alpha}_n > 1$ and the corresponding modes are cut off). Among these modes, only the TE_{01} mode, presenting the lowest losses ($\cong 2\times 10^{-3}$ dB/m), is excited in our experimental arrangement (see Sec. III B). $\bar{\alpha}_1$ is about 4° and the guided wavelength $\lambda_1 = 2\pi/k_1$ departs from the free-space wavelength $\lambda_0 = 2\pi/k_0$ by only 0.25%.

Figure 6 gives the corresponding distribution of the electric field. Note that this distribution (as for all the TE_{0n} modes) is unvarying in a rotation around the axis Oz but that, in each point, the electric field is linearly (not circularly) polarized. The power transmission of the waveguide elements is 0.92 per single trip of 182 m, but, as a result of unavoidable localized losses (see Sec. III B), the actual transmission of the cell falls to $A_0 \cong 0.724$ (1.4 dB). The power transmission of the Fabry-Pérot cavity, filled with a linear medium of power absorption coefficient α and of refractive index n_i, is easily derived by standard procedures.[65] We get

$$\mathcal{T} = \frac{A_0 e^{-\alpha l} T_0^2}{1 + A_0^2 R_0^2 e^{-2\alpha l} - 2 A_0 R_0 e^{-\alpha l}\cos\varphi} , \tag{3.7}$$

where, taking account of the waveguide oversizing and assuming $|n_i - 1| \ll 1$ (as usual, in low-pressure gases), the phase φ reads

$$\varphi = 2 k_1 n_i l . \tag{3.8}$$

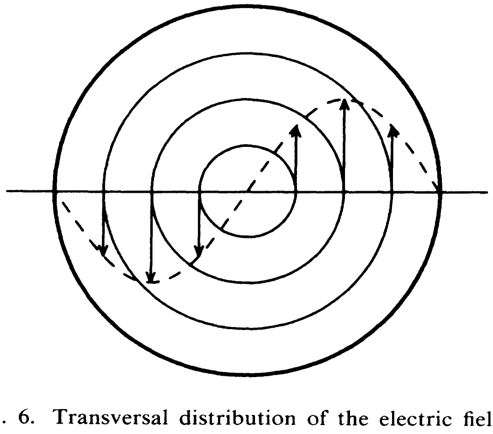

FIG. 6. Transversal distribution of the electric field in the TE_{01} mode along a diameter of the waveguide.

This transmission is identical to that of the same cavity without cell losses ($A_0 = 1$) provided that R_0 and T_0 are replaced by the effective coefficients $R = R_0 A_0 = 0.69$ and $T = T_0\sqrt{A_0} = 0.043$. The resonance of the empty cavity are characterized by a finesse F

$$F = \pi\sqrt{R}/(1-R) \cong 8.4 \tag{3.9}$$

corresponding to a mode width of 49 kHz (HWHM) and a photon lifetime $\tau \cong 3.2$ μs. The transmission on resonance and antiresonance are, respectively, $T^2/(1-R)^2 = 1.86\times 10^{-2}$ (-17.3 dB) and $T^2/(1+R)^2 = 6.31 \times 10^{-4}$ (-32 dB).

As we said in Sec. II, we simulate the experimental situation by the equivalent ring cavity (ERC) of Fig. 1(b). In our calculations we fix $R = 0.69$ and $T = 0.043$ so that $T + R = 0.733 < 1$. The ERC filled with $HC^{15}N$ is characterized by a cooperativity parameter $C = \alpha_\infty l F / 2\pi > 200$ that is much beyond the threshold of bistability ($C = 4$ in the mean-field limit[42]). In the absence of gas, the amplitude E_c^0 of the intracavity field in resonance reads

$$E_c^0 = E_i \sqrt{T}/(1-R) , \tag{3.10}$$

where E_i is the amplitude of the input incident field. E_i and A_0 being given, note that the conditions of a high cavity finesse (requiring $R_0 \rightarrow 1$) and of a large intracavity field are conflicting ($E_c^0 = 0$ for $R_0 = 1$). The value $R_0 = 0.95$ may be considered as a good compromise, leading to a finesse $F = 8.4$ not far from its upper bound ($F = 9.7$ for $R_0 = 1$) and to a reasonable ratio $E_c^0/E_i \cong 0.67$.[66]

In principle, the equivalence between the ERC and the real Fabry-Pérot cavity breaks down when the intracavity medium is nonlinear. This results from the inhomogeneity of the field distribution (longitudinal, mainly related to standing waves, and transversal, related to the mode structure). Another possible effect is the generation in the absorber of other modes TE_{0n} that the initially excited TE_{01} mode. However, the waveguide losses significantly increase with the mode number n; only the TE_{01} mode is coupled to the detection (see Sec. III B) and, as a result of the strong saturation of the medium, the relative absorption per round trip in the cavity remains moderate in the conditions where instabilities were observed (upper branch of the bistability curve). It is then expected that the higher-order transverse modes play no significant role. In fact, the nonlinear behavior of the real system turns out to be similar to that of the ERC.

B. Experimental arrangement

Figure 7 gives a diagram of the Fabry-Pérot cavity used in the experiments.[36] Due to space limitations, the 182-m-long waveguide cell was split in two approximately 91-m-long straight sections and folded by means of two 90° mitre elbows. Each section included eight elements of helix waveguide,[62] carefully lined in order to reduce the losses resulting from mode conversion. The waveguide elements, manufactured by the Société Anonyme des Télécommunications, are high-quality aluminum tubes,

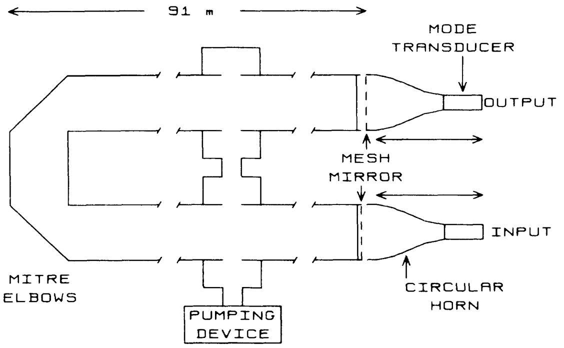

FIG. 7. Diagram of the cavity.

the inner wall of which are covered successively by a 180-μm-thick Mylar sheet and by a close-wound solenoid in insulated copper wire, of pitch equal to the wire diameter and of the inner diameter $\phi = 60 \pm 0.02$ mm. This structure provides a very low attenuation for the TE_{0n} modes (2×10^{-3} dB/m for the TE_{01} mode at $\lambda \cong 3.5$ mm) and a very large absorption for the other modes (up to 200 dB/m).

The waveguide cell was closed by two windows (not shown in Fig. 7) in compressed Kel-F (polychlorotrifluoroethylene). Their thickness $e \cong 1.2$ mm was chosen such that $n_l e \cong \lambda_0/2$, in order to present spurious reflections on the windows. Note that the windows have to support a differential pressure of about 1 atm on an area approximately 30 cm^2. Among the transparent materials having the required mechanical strength we retained *compressed* Kel-F because of its negligible birefringence. The cell was evacuated through eight holes of 16-mm diameter drilled in two short sections of circular waveguide, inserted in the medium of each straight section of the helix waveguide and having the same inner diameter ($\phi = 60$ mm). The large apertures in the walls of the waveguide (total area of about 16 cm^2) were necessary to achieve a reasonable pumping time of the cell. Fortunately, due to the oversizing of the waveguides, they do not entail dramatic microwave losses. Two other short sections of circular waveguide were inserted close to the input and output vacuum windows. They communicated through a single hole of small diameter (2 mm) with the adjustable leak used to introduce the $HC^{15}N$ gas and with the pressure gauge. After one month of continuous pumping, necessary to evacuate most volatile materials, the total rate of degazing and residual leak was about $1.6 \times 10^{-4} l$ Torr/s for the whole cell (volume of about $520 l$) and the minimum pressure attained at the end of the cell, that is 45 m away from the pump, was about 6×10^{-5} Torr. A time of about 15 min was required to bring the pressure at this point from 60 to 0.1 mTorr.

The $HC^{15}N$ gas used in our experiments was synthetized in the laboratory by reaction of phosphoric acid on potassium cyanide $KC^{15}N$.[67] No attempt was made to obtain pure $HC^{15}N$. The composition of the gas, determined by gas-phase chromotography and by mass spectrometry, was approximately as follows: $HC^{15}N \cong 81\%$, $H_2O \cong 12\%$, $N_2 \cong 6\%$, $O_2 \cong 1\%$. Note that the main impurities have no lines close to the 0-1 line of HCN. The pressure broadening coefficient of 22.75 kHz/mTorr was determined on $HC^{15}N$ prepared by the same technique.[57] The gas optical thickness is too large to be measured by standard techniques. It was indirectly determined from the analysis of the transient pulse transmitted by the gas subjected to an incident stepwise field on resonance (see Fig. 8 and Ref. 61). This gives access to the quantity $\alpha_\infty l / T_2$ (related to the superradiant time) from which we derived $\alpha_\infty = 1 \pm 0.1$ m^{-1}. The gas pressure was measured by a well-compensated, high-sensitivity Pirani gauge, including four elements mounted in a Wheatstone bridge, two being connected to the cell and the other two evacuated and sealed off with a getter. This gauge was calibrated on an absolute capacity gauge. The pressure read is exact for air but a recent calibration with our $HC^{15}N$ samples showed that it has to be multiplied by a factor 0.70 for this gas.[68]

The overall attenuation of the empty waveguide cell in the TE_{01} mode was measured to be 1.4 dB (corresponding to a transmission $A_0 = 0.724$), roughly distributed as follows: 0.6 dB in the mitre elbows (due to unavoidable mode conversion[69]), 0.3 dB in the circular waveguide elements, 0.2 dB in the helix waveguide, 0.2 dB in the joining of the different waveguide elements, and 0.1 dB in the vacuum windows. The cell was transformed into a cavity by adding two identical mesh mirrors, made of 330-μm-thick plates in gilded copper, drilled of circular holes (diameter 1.1 mm) according to an hexagonal pattern (period 1.6 mm). The reflexion and transmission coefficients (respectively, $R_0 = 0.95$ and $T_0 = 0.05$) of these mirrors were derived from measurements of the cw transmission of the empty cavity on resonance (-17.3 dB) and from the study of its transient response to a stepwise field (Fig. 9).

The selective excitation of the cavity in the TE_{01} mode raises a difficult problem related to the waveguide oversizing. We used a three-component device including the

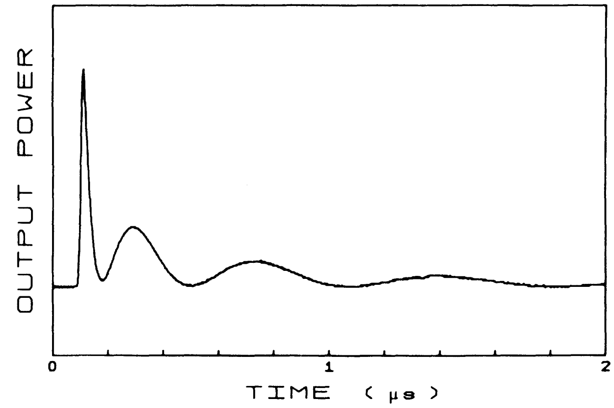

FIG. 8. Transient signal transmitted by a 182-m-long sample of $HC^{15}N$ at 0.98 mTorr subjected to an incident step on resonance. $\alpha_\infty l / T_2$ may be derived from the zeroes of the signal, observed, respectively, at times 2.89, 15.2, and 37.4 $T_2 / \alpha_\infty l$ (see Refs. 61 and 68).

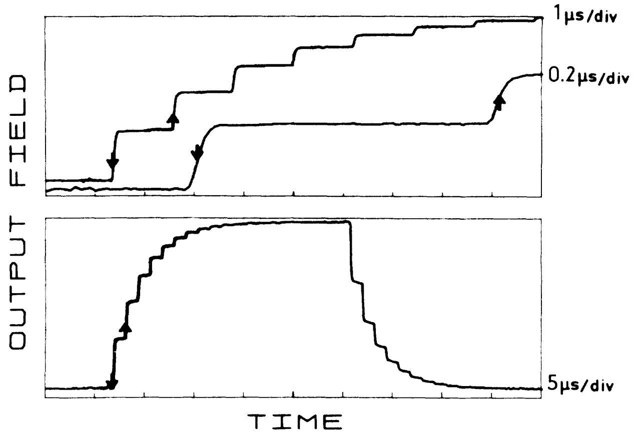

FIG. 9. Transient response of the cavity on resonance to a square-wave modulation of the input field and enlargements of parts of this curve. From up to down, the time scales are 1, 0.2, and 5 μs per division. The duration of each step of the staircase is obviously that of a round-trip time in the cavity ($\simeq 2l/c \simeq 1.2$ μs) whereas the overall rise and fall times give the photon lifetime in the cavity ($\tau \simeq 3.2$ μs). Note that the detection is here linear, the modulation index being very low. The ratio of the heights of two successive steps is then equal to $R \simeq 0.69$.

following: a mode transducer of type King[70] (Hitachi W 6414), achieving the transition from the TE_{10} mode of the standard rectangular waveguide WR 10 to the TE_{01} mode of an intermediate circular waveguide of inner diameter 5.50 mm, such that the modes TE_{0n} with $n > 1$ are cut off; a short section of helix waveguide (inner diameter 5.5 mm), acting as a mode filter eliminating the residuals of all other modes; a 1-m-long circular horn achieving the transition to the diameter $\phi = 60 \pm 0.02$ mm, of bottlelike shape, specially designed[71] to keep the possible excitation of the modes TE_{0n} (with $n > 1$) 40 dB below that of the mode TE_{01}. The overall attenuation of the three elements is about 1.3 dB. An identical device was used to select the TE_{01} mode in the beam transmitted through the output mirror. The input (output) mirror was tied to the waveguide cell (the output horn; see Fig. 7). The two circular horns were mounted on translation units, driven by micrometer heads enabling us to tune the resonance frequency of the cavity and to optimize the input coupling.

The input millimetric wave was supplied by a klystron delivering a maximum power of the 500 mW. The klystron was phase locked by standard techniques, eliminating the frequency drifts and reducing the field spectrum bandwidth down to about 1 kHz (HWHM). Any feedback from the cavity to the source was prevented either by an isolator associated to a low-loss narrow-band Y-junction circulator or by two circulators. In some experiments, the power was controlled by a *p-i-n* diode modulator. Due to the attenuation of the different elements introduced between the source and the input mirror, the maximum power actually reaching the latter ranged from 60 to 170 mW, depending on the experimental arrangement. The source parameters were controlled by a synthesizer–function-generator (HP 3325 A), programmed by a microcomputer. In the frequency-swept experiments, it was used in its synthesizer function as intermediate frequency (IF) reference in the phase-locking system where the continuity of its phase during the frequency switchings is an invaluable advantage. In the experiments where the input power is the control parameter, it was used as a function generator of high resolution (four digits) to drive the *p-i-n* modulator. At the other end of the cavity, the transmitted wave was received on a Schottky diode mixer, through a Y-junction circulator. The signal delivered by the mixer, proportional to the transmitted power (quadratic detection), was sent on a two-channel digital oscilloscope (Lecroy 9400), capable of storing 32 000 points on each channel, with a time resolution up to 10 ns and a nominal (effective) vertical resolution of 8 (6.5) bits in single shot operation. The second channel was used to record the experimental parameters and the data collected on both channels were transferred to the microcomputer for further processing or drawing.

In some experiments the quadratic video detection described above has been replaced by an heterodyne detection in order to analyze more precisely the spectrum of the signal transmitted by the cavity. The signal was then introduced in the coupling arm of a 10-dB directional coupler, whereas the power delivered by a subharmonic local oscillator was sent in the main arm. The local oscillator was also a klystron, phase locked at a frequency $\nu_{lo} \simeq 43$ GHz such that $\nu_0 = 2\nu_{lo} + f_i$ with $f_i \simeq 90$ MHz, and the beat delivered by the Schottky diode mixer was sent on a spectrum analyzer Advantest model TR4131. The power of the local oscillator applied to the mixer was always kept at least 20 dB beyond that of the signal in order to ensure a linear detection of the latter. The spectrum obtained around f_i is then a simple transposition of the signal spectrum around ν_0.

C. Experimental results

Figure 10 gives an example of bistability cycle, evidencing a well-developed self-pulsing on its upper branch.

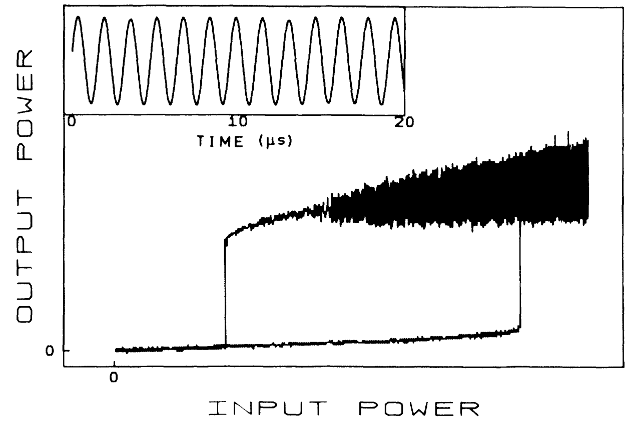

FIG. 10. Bistability cycle observed for $\nu_p = \nu_m$, $\nu_m - \nu_0 = -317$ kHz. Gas pressure $p \simeq 0.53$ mTorr (see Ref. 68). Inset: sine-wave self-pulsing obtained when the incident power is fixed at its maximum. The time scale is only indicative (uncalibrated).

It has been obtained by slowly sweeping the input power, controlled by the *p-i-n* modulator. The molecular frequency ν_m coincides with that of a longitudinal mode of the cavity ν_p but differs from the source frequency ν_0. For a fixed input power (cw excitation), the self-pulsing is almost purely sinusoidal (see inset of Fig. 10) and its frequency ν_{sp}, of the order of 600 kHz, does not significantly vary inside the instability region. The sinusoidal nature of the self-pulsing has been verified in all our experiments. A spectral analysis shows only the presence of harmonic 2 at a very low level (more than 30 dB below the main component) but no evidence of subharmonics. This point is discussed more extensively at the end of this section.

Except obviously for the self-pulsing, the hysteresis cycle of Fig. 10 is fairly well (within 30%) fitted by the steady-state bistability curve of the equivalent ring cavity (ERC) defined in Sec. II, computed in the plane-wave approximation [see Eq. (2.9)] without any adjustment of the experimental parameters. This surprising agreement has been confirmed on hystersis cycles obtained in different conditions.[72] It may be improved by slightly adjusting the optical thickness $\alpha_\infty l$ of the gas, taking 146 instead of 182 ± 18. The ratio of the upper (P_u) and lower (P_l) switching powers in Fig. 10 is then exactly reproduced. For the maximum input power, the Rabi frequencies, derived from the calculations on the ERC, are $\nu_{ri}=1.33$ MHz and $\nu_r=0.45$ MHz just before the input and output mirrors, respectively. Note that ν_{ri} so calculated is consistent with the estimates of the corresponding input power (80 ± 30 mW), this showing the accuracy of the model.[73]

Though the recording time of Fig. 10 was about 1 s, dynamical effects are probably present, especially in the vicinity of the turning point (where the self-pulsing disappears) for which the response times become very long. In order to study more quantitatively the dependence of the self-pulsing on the incident power, we have performed experiments in which the input power, starting from its maximum value, is lowered step by step with a long stabilization time provided after each step before the measurements allowing the steady state to be reached. The procedure has been fully automatized in order to keep a reasonable duration of the data collection and to prevent drifts of the experimental parameters (cavity tuning, gas pressure, etc., . . .). At the end of each stabilization time, the self-pulsing frequency and the upper and lower levels of the oscillations are measured during a short time (≈ 10 μs). Figure 11 shows a recording obtained by this technique, with 124 steps, a stabilization time of 0.25 s and then an overall duration of the recording of about 32 s. The fact that the self-pulsing frequency ν_{sp} is almost independent of the incident power is confirmed [Fig. 11(a)], its variations in the region explored being below the experimental uncertainty. A new point is that the distribution of the oscillation extrema is well fitted by a parabola [Fig. 11(b)], as expected in the vicinity of a supercritical Hopf bifurcation.[74] This feature was hidden on the recording of Fig. 10 by dynamical effects which artificially extend the oscillations outside the instability region.

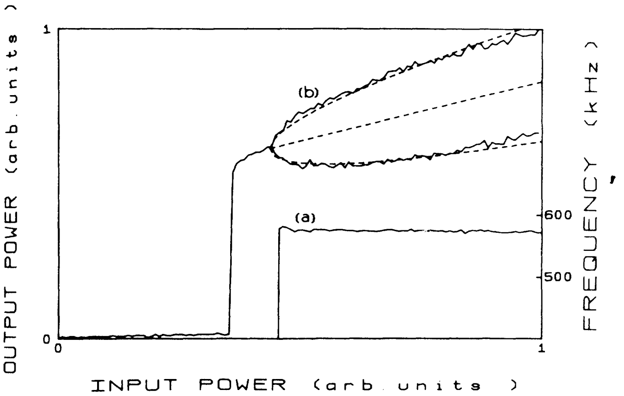

FIG. 11. Quantitative study of the dependence of the self-pulsing parameters on the incident power. (a) Frequency; (b) distribution of the oscillation extrema (dotted line: parabola achieving the best fit). Experimental conditions: $\nu_p=\nu_m, \nu_m-\nu_0\cong 300$ kHz, $p=0.60$ mTorr, maximum power as in Fig. 10 ($\nu_{ri}=1.33$ MHz).

In all our experiments, self-pulsing has been observed only in the presence of bistability and in the upper branch of the bistability curve. By the standard procedure consisting of sweeping the input power, this branch is attained only when the available input power P_i is larger than the upper switching power P_u. P_u is strongly dependent on the experimental parameters, especially the molecular detuning $\nu_m-\nu_0$. A much wider domain of instability can thus be explored by use of the source frequency ν_0 as control parameter.[75,76] Starting from a detuning such that P_u is low, it is indeed possible to follow by continuity the upper branch of the bistability curve as long as P_i is larger than P_l which may be one order of magnitude lower than P_u on account of the large value of the bistability parameter C (see Sec. IV). Moreover, by removal of the *p-i-n* modulator, no longer required, the input field can be significantly enhanced.

Figure 12 has been obtained in these conditions for $\nu_m=\nu_p$. Curve *a*, given for reference, shows three successive TE_{01} modes of the empty cavity. Note the absence of parasitic modes. With introduction of the HC^{15}N gas, self-pulsing is observed for source frequencies ranging from 150 to 370 kHz apart from the molecular frequency ν_m, on each side of this one. Note that, for suitable detunings of the source, the peak-to-peak amplitude of the oscillations may be of the order of the average signal detected. For $p=0.98$ mTorr (curve *d*) the bistable system switches down when P_l becomes larger than P_i and switches up back only when P_u becomes smaller than P_i. The symmetric curve is obviously obtained reversing the frequency sweep.[72] At too high pressures (depending on P_i), the condition $P_l<P_i$ is no longer fulfilled inside the instability domain and the self-pulsing cannot be observed.

The shapes of the curves of Fig. 12 and, in particular, the frequencies at which the switchings occur, are very sensitive to the values of the physical parameters. A good fit between the experimental data and those calculated for the ERC (see Sec. IV) is obtained by taking

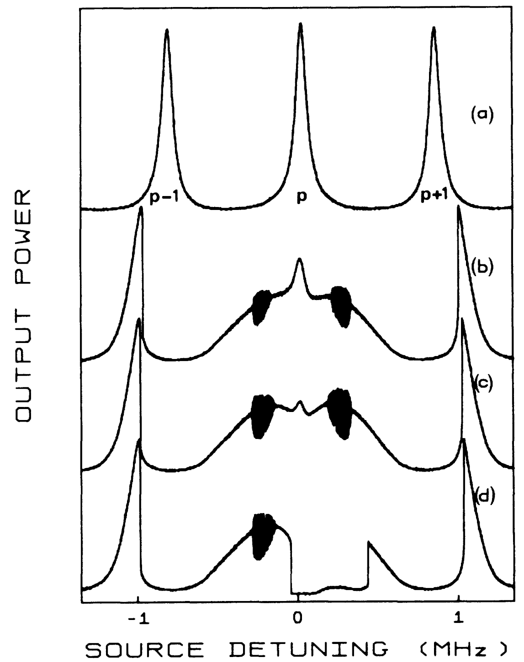

FIG. 12. Power transmitted by the cavity vs $\nu_0-\nu_m$ for $\nu_m=\nu_p$ and $p\cong 0$ mTorr (curve *a*), 0.91 mTorr (curve *b*), 0.95 mTorr (curve *c*), and 0.98 mTorr (curve *d*) (see Ref. 68). The input power P_i is such that $\nu_{ri}=1.44$ MHz.

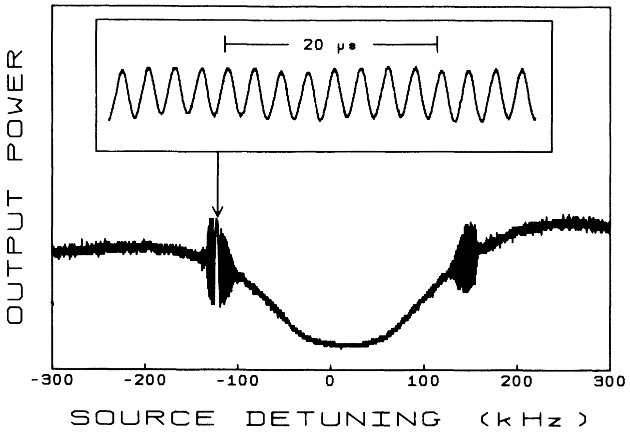

FIG. 13. Self-pulsing in an antiresonant configuration. The output power is plotted vs $(\nu_0-\nu_m)$ for $\nu_m=(\nu_p+\nu_{p+1})/2=\nu_p+c/4l$, $p=0.60$ mTorr, $\nu_{ri}=1.44$ MHz. Note that the wiggle on the curve is an artifact resulting from the sampling procedure. Inset: self-pulsing for $\nu_0-\nu_m=127$ kHz ($\nu_{\text{sp}}=400$ kHz).

$\alpha_\infty l=146$ as previously and $\nu_{ri}=1.44$ MHz, a value again quite consistent with the estimated incident power. From ν_{ri} it is easy to derive the Rabi frequency inside the empty cavity on resonance $\nu_r=\nu_{ri}\sqrt{T}/(1-R)\cong 0.96$ MHz [see Eq. (3.10)] and then, all the recordings being obtained with the same sensitivity, to determine ν_r in any point from the corresponding amplitude of the detected signal. The r.m.s. value of ν_r turns out to be nearly constant in the instability regions of curves *b*, *c*, and *d* ($\nu_r^{(2)}\cong 630$ kHz) and comparable to the self-pulsing frequency ($\cong 670$ kHz). Moreover, the ratio of the cavity transmissions, with and without gas, enables us to give an estimate of the gas absorption per passage. We get a small value ($\langle\langle\alpha l\rangle\rangle_{\text{av}}\cong 0.15$), as expected because of the strong saturation of the molecular line.

For a given input power P_i, the most robust oscillations are observed when the molecular frequency ν_m coincides with the frequency ν_p of a resonance of the empty cavity ("resonant configuration") and when the gas pressure is close to the highest value such that there exists an overlapping of the region where $P_i>P_l$ with the instability region. These conditions are fulfilled in Fig. 12, but self-pulsing can be observed in quite different conditions. As an example, Fig. 13 shows oscillations obtained in the extreme case where the molecular frequency ν_m is just halfway between two resonances of the empty cavity ("antiresonant configuration"). Let us emphasize that, even in this case, (i) the system is bistable with respect to the incident power and the self-pulsing appears on the upper branch of the corresponding hysteresis cycle, and (ii) the gas absorption remains moderate in the instability region ($\langle\alpha l\rangle_{\text{av}}<1$). Note again that the intracavity Rabi frequency in this region ($\nu_r^{(2)}=260$ kHz) is of the same order of the oscillation frequency ($\nu_{\text{sp}}\cong 400$ kHz).

The theory of the multimode instability predicts that self-pulsing occurs in a restricted domain of input power.[42] The upper bound of this domain cannot generally be attained with the microwave power delivered by our source. However, the existence of an optimum input power leading to a maximum of the self-pulsing amplitude has been evidenced in particular conditions. Figure 14 shows the result of an experiment where self-pulsing is observed for incident Rabi frequency ranging from 1.28 to 1.81 MHz. The frequency of the oscillations is nearly constant in this domain (690±10 kHz). An important

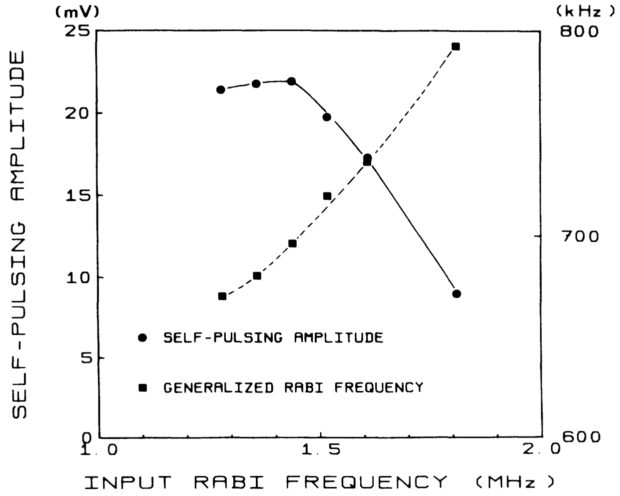

FIG. 14. Dependence of the self-pulsing amplitude and of $\nu_r^{(4)}$ on ν_{ri} for $\nu_m-\nu_0=270$ kHz, $\nu_m-\nu_p=95$ kHz, $p=0.75$ mTorr.

point is that their amplitude is maximum when their frequency coincides with the generalized Rabi frequency $\nu_r^{(4)}$ inside the cavity. This result is clearly related to the fact that the Raman gain is maximum at $\nu_0-\nu_r^{(4)}$ when $\nu_m > \nu_0$ (Ref. 26) (see the second rule of thumb in Sec. II).

In order to study more systematically the dependence of the self-pulsing frequency $\nu_{\rm sp}$ on the physical parameters, experiments have been achieved in different configurations and in various experimental conditions. We note first that the self-pulsing frequency $\nu_{\rm sp}$ does not significantly depend on the gas pressure, at least in the instability regions attainable with the available input powers. Our attention has been then focused on the influence of the molecular and cavity detunings and of the intracavity Rabi frequency.

Recordings obtained in detuned configurations for fixed values of the gas pressure and of the incident power are presented Fig. 15. The recording *c* corresponds to the resonant configuration. It allows us to define unambiguously the central mode p ($\nu_p=\nu_m$) and the side modes $p\pm1$ of the empty cavity. When the cavity is detuned from ν_m it is easy to follow by continuity these modes which remain well defined. The recordings of Fig. 15 are extracted from a series and, for a given source frequency, it is possible to derive the intracavity Rabi frequency from the level of the detected signal and to measure the frequency $\nu_{\rm sp}$ of the self-pulsing. The results obtained for $\nu_0=\nu_m-240$ kHz are shown Fig. 16. The measured self-pulsing frequency $\nu_{\rm sp}$, $\nu_{\rm th}^{(1)}=|\nu_0-\nu_{p-1}|$, the Rabi frequencies $\nu_r^{(1)}$ and $\nu_r^{(2)}$, the generalized Rabi frequencies $\nu_r^{(3)}$ and $\nu_r^{(4)}$ are plotted versus the cavity detuning $\nu_p-\nu_0$. The closeness of all these curves shows that the rules of thumb discussed in Sec. II provide a good tool for the interpretation of the experimental results. As mentioned in Sec. II $\nu_r^{(1)}$ and $\nu_r^{(3)}$, which correspond to unstable stationary solutions, cannot be determined experimentally. They have been estimated by prolonging by continuity the recordings from the stable regions to the unstable ones.

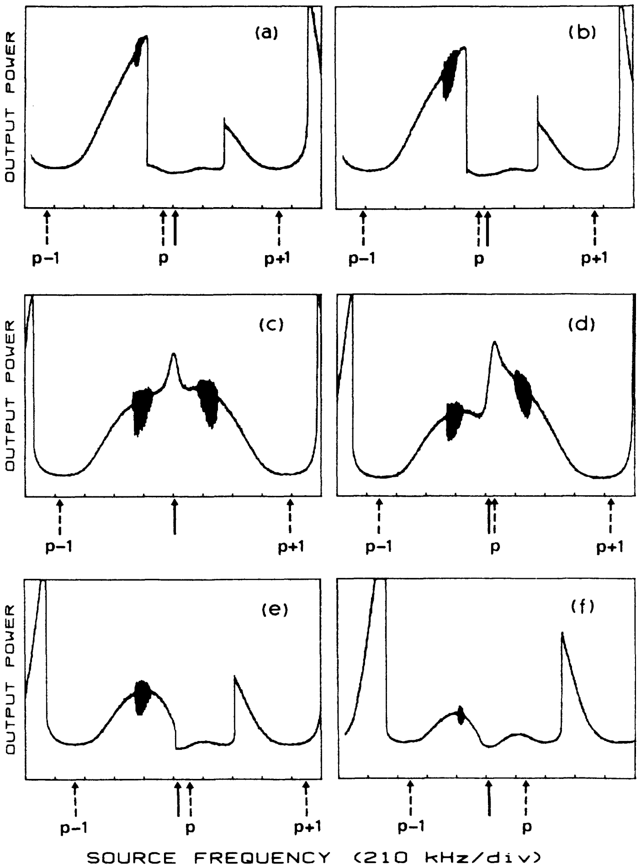

FIG. 15. Self-pulsing in detuned configurations. The dotted and solid arrows, respectively, indicate the modes of the empty cavity and ν_m. The output power is plotted vs ν_0 (unit: 210 kHz) for $p=0.70$ mTorr, $\nu_{ri}=1.44$ MHz, $\nu_p-\nu_m=$(a) −90 KHz, (b) −62 KHz, (c) 0 KHz, (d) 47 KHz, (e) 90 KHz, and (f) 265 kHz.

The previous results have been obtained for a single value of the molecular detuning. In order to explore a wider experimental domain, we have developed a semiautomatized procedure where only $\nu_{\rm sp}$ and the r.m.s. detected signal (giving $\nu_r^{(2)}$ and $\nu_r^{(4)}$) are measured. Moreover, the arrangement of the experiment has been slightly modified in order to increase the incident field ($\nu_{ri}\cong1.81$ MHz). Note that self-pulsing has never been observed when $\nu_0=\nu_m$ (purely absorptive bistability).

In Figures 17–19, the experimental data collected for six positive values of the molecular detuning $\nu_m-\nu_0$ are directly compared to the predictions of the rules of thumb discussed in Sec. II. In Fig. 17 $\nu_{\rm sp}$ is plotted versus $\nu_{\rm th}^{(1)}=|\nu_{p-1}-\nu_0|$ where ν_{p-1} is the frequency of the side mode of the empty cavity for which the gain of the medium may be positive ($\nu_{p-1}<\nu_0<\nu_m$).[77] The departures of the measured points from the bisectrix give a direct insight into the validity of the first rule of thumb. These departures are in general quite moderate (<25%). They become negligible for the highest oscillation fre-

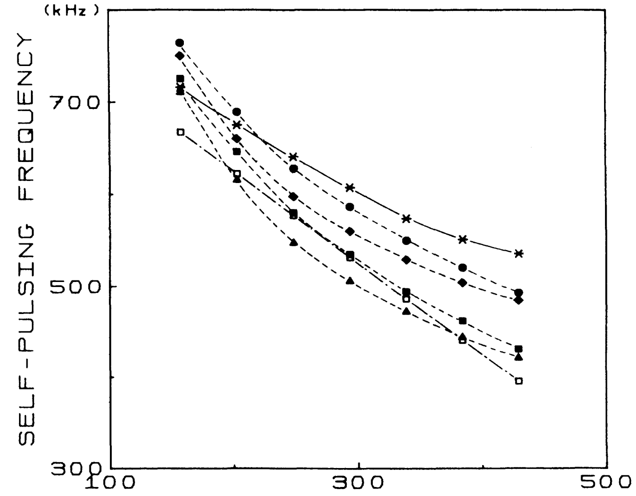

FIG. 16. $\nu_{\rm sp}$ vs ($\nu_p-\nu_0$) in the conditions of Fig. 15 for $\nu_m-\nu_0=240$ kHz: (✱) experimental results, (□) $\nu_{\rm th}^{(1)}$, (■) $\nu_r^{(1)}$, (▲) $\nu_r^{(2)}$, (●) $\nu_r^{(3)}$, (◆) $\nu_r^{(4)}$.

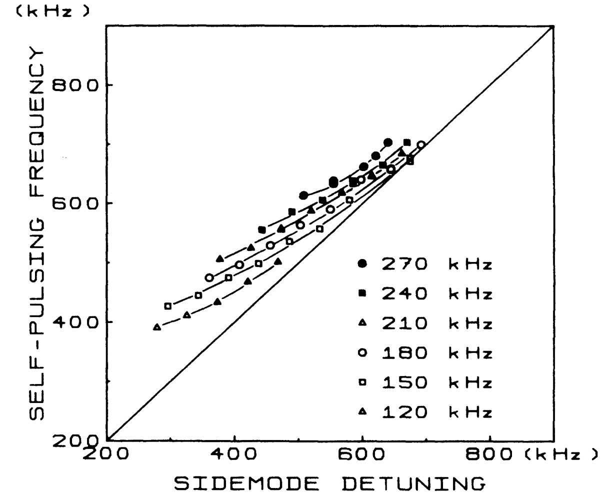

FIG. 17. Comparison of the self-pulsing frequency ν_{sp} with the predictions of the first rule of thumb for $p = 0.9$ mTorr, $\nu_{ri} = 1.81$ MHz. The symbols relate to the values of the molecular detuning $(\nu_m - \nu_0)$ described in the inset.

quencies, that is, when the Rabi frequency is large (see Fig. 19) and the saturation is strong. The medium being then nearly transparent and amplifying in a region wider than the cavity linewidth, it is not surprising that the frequency of the oscillations is fixed in this case by the resonance of the empty cavity. The second rule of thumb prescribes that the self-pulsing frequency ν_{sp} has to be of the order of the intracavity Rabi frequency. Figures 18 and 19 show that the measurements are in fairly good agreement with the prediction, regardless of the Rabi frequency considered (generalized or not). Recall that in a homogeneously broadened medium[26] the Raman gain is maximum at $\nu_0 - \nu_r^{(4)}$ (for $\nu_0 < \nu_m$), whereas numerical calculations on a Doppler-broadened medium[47] have shown that this maximum may occur at $\nu_0 - \nu_r^{(2)}$. In fact, $\nu_r^{(2)}$ and $\nu_r^{(4)}$ are not significantly different in our experiments. The second rule of thumb is perfectly verified for intermediate values of the Rabi frequency (around 80% of its maximum). We have experimentally observed that the self-pulsing amplitude is maximum in these points. When the intracavity field increases, the region of net gain widens and the self-pulsing frequency is no longer mainly fixed by the gain peak condition. This may explain the departures observed for the highest Rabi frequencies. This interpretation is well confirmed by the recording of Fig. 14 where, by reducing the input power, a maximum of the oscillations have been observed when their frequency becomes equal to $\nu_r^{(4)}$. On the contrary, the gain peak condition is expected to be determinative at low Rabi frequency. Note, however, that the medium is far from being optically thin in this case. The apparent departures from the second rule of thumb may then be attributed to the fact that the Rabi frequency averaged on the whole cavity is significantly larger than that measured just before the output mirror, used in plotting Figs. 18 and 19.

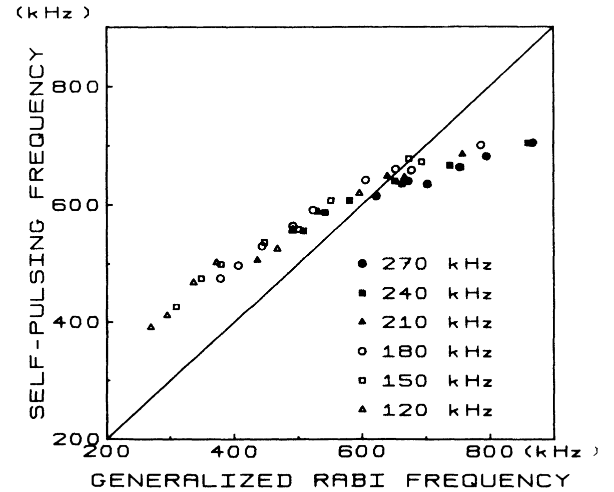

FIG. 18. Comparison of ν_{sp} and $\nu_r^{(4)}$. Other conditions as in Fig. 17.

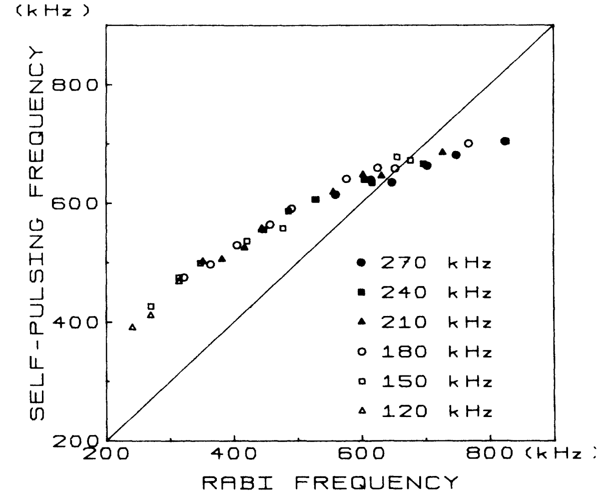

FIG. 19. Comparison of ν_{sp} and $\nu_r^{(2)}$. Other conditions as in Fig. 18.

To summarize the previous discussion, all our results turn out to bring an experimental support to the sidemode gain model of which the rules of thumb are a simplified formulation obtained by disregarding the transversal and longitudinal distribution of the field and neglecting possible shifts of the relevant side mode resulting from induced changes of the refractive index (see Sec. II). In this model, the self-pulsing is seen as the beat note between the driving frequency ν_0 and a single frequency $\nu_0 \pm \nu_{sp}$. However the video detection, considered up to now, cannot discriminate between this situation and another one where the driving field would be amplitude modulated at the frequency ν_{sp}. We have then achieved a spectral analysis of the field transmitted by the cavity with the linear heterodyne detection described at the end of Sec. III B. Figure 20 gives a typical spectrum. The molecular detuning $\nu_m - \nu_0$ and the self-pulsing frequency ν_{sp} are, respectively, 270 kHz and 645 kHz. The verti-

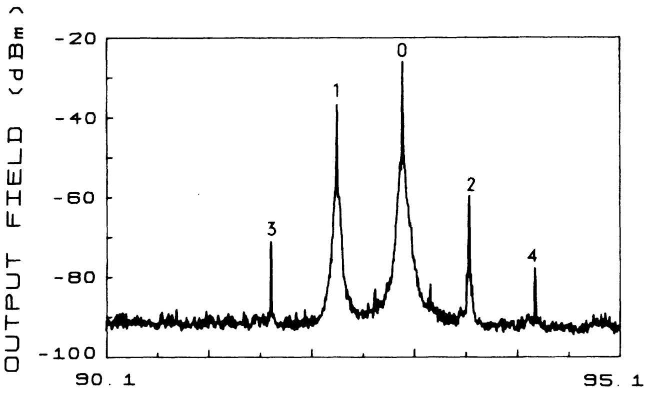

FIG. 20. Spectrum of the field transmitted by the cavity for $p = 1.33$ mTorr, $\nu_{ri} = 1.81$ MHz, $\nu_m - \nu_0 = 270$ kHz. Vertical scale: 10 dB per division. The frequency increases from left to right (500 kHz per division). The different components correspond to field frequencies equal to (0) ν_0, (1) $\nu_0 - \nu_{sp}$, (2) $\nu_0 + \nu_{sp}$, (3) $\nu_0 - 2\nu_{sp}$, (4) $\nu_0 + 2\nu_{sp}$, with $\nu_{sp} = 645$ kHz.

cal scale is logarithmic and, because of our good signal-to-noise ratio we can explore a range of 60–70 dB, significantly larger than that attained in the optical experiments.[46,47] As expected, two frequencies prevail, ν_0 and $\nu_0 - \nu_{sp}$, the latter being located on the side of ν_0 for which the medium can amplify ($\nu_0 - \nu_{sp} < \nu_0 < \nu_m$; see Fig. 2). The sideband amplitude is about 10 dB below that of the driving field. Additional components at the frequencies $\nu_0 + \nu_{sp}$, $\nu_0 - 2\nu_{sp}$, and $\nu_0 + 2\nu_{sp}$ appear in the spectrum of Fig. 20 at a level more than 20 dB below the main sideband involved in the side-mode gain model. We have carefully verified that these additional components are not artifacts generated in the mixer used to the heterodyne detection. In this purpose the field transmitted by the cavity has been attenuated and we have only observed the same attenuation on the whole spectrum of Fig. 20 without any change of the relative amplitudes of its different components. This confirms that our heterodyne detection is actually linear with respect to the field transmitted and that the additional components are actually present in this field. This presence may be explained by multiwave processes in the medium, subjected simultaneously to the frequencies ν_0 and $\nu_0 - \nu_{sp}$. On account of their low level and of the ratio of the transmission of the cavity on resonance and on antiresonance ($\cong 15$ dB), their generation does not require a resonance of the cavity, contrary to the main sideband at $\nu_0 - \nu_{sp}$. Note also the presence of very small features in the pedestal of the main peak at ν_0. They are at the limit of our detection sensitivity and it is difficult to say if they correspond to the generation of possible self-pulsing subharmonics in the medium or to parasites.

As indicated previously, the signal obtained with the video detection contains a main component at ν_{sp} and a weak component at $2\nu_{sp}$. They result, respectively, from the beat note between ν_0 and $\nu_0 - \nu_{sp}$ and between $\nu_0 - \nu_{sp}$ and $\nu_0 + \nu_{sp}$. Assuming that the video detection is quadratic, it is easy to predict from the spectrum of Fig. 20 the relative amplitude of the components at ν_{sp} and $2\nu_{sp}$. We get 34 dB, a value in good agreement with the observations. This confirms the correctness of our interpretations.

IV. NUMERICAL RESULTS

In order to solve numerically the Maxwell-Bloch equations (2.1) with the boundary conditions (2.4) we exploited the same program used in Ref. 78, generalized to include the presence of the driving field. In the results that we illustrate in this section, we select the following values for the parameters:

$$\begin{aligned} &\alpha l = 146, R = 0.69, T = 0.043 \;, \\ &\frac{c}{2l} = 830 \text{ kHz} \;, \qquad (4.1) \\ &\gamma_{\parallel}/2\pi = \gamma_{\perp}/2\pi = 22.75 \text{ kHz/mTorr} \;, \end{aligned}$$

while the remaining parameters, i.e., the Rabi frequency ν_{ri} of the input field, the pressure, the molecular and cavity detunings change from diagram to diagram. With the exception of αl, all the values specified in Eq. (4.1) correspond closely to the experimental situation. The value of αl given in (4.1) is smaller than the experimental one by a factor approximately equal to 0.7; we selected it to fit the experimental value of the ratio of up-switching power to down-switching power obtained, for example, from Fig. 10.

Let us discuss first the two rules of thumb introduced in Eq. (2.12) and (2.13). In Figs. 21 and 22 the pressure is $p = 0.75$ mTorr, and the cavity is exactly resonant with the molecules, i.e., $\nu_m = \nu_p$. The Rabi frequency of the input field is 1.42 MHz in Fig. 21 and 1.29 MHz in Fig. 22. Over a wide interval of the detuning, these diagrams compare the numerical value of the oscillation frequency with the quantities $\nu_{th}^{(1)}, \nu_{th}^{(2)}, \nu_r^{(1)}, \nu_r^{(2)}, \nu_r^{(3)}, \nu_r^{(4)}$ defined in Sec. II in connection with the two prescriptions (2.12)

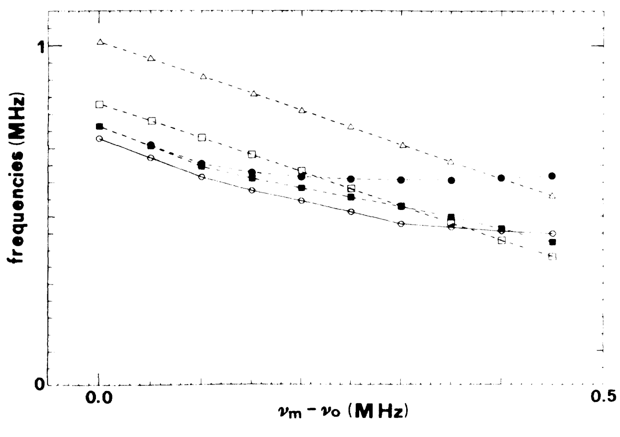

FIG. 21. The parameters not specified in Eq. (4.1) are $p = 0.75$ mTorr, $\nu_{ri} = 1.42$ MHz. As a function of the detuning parameter $\nu_m - \nu_0 = \nu_p - \nu_0$, the figure shows (○) the oscillation frequency, numerically obtained from the Maxwell-Bloch equations, (□) $\nu_{th}^{(1)}$, (△) $\nu_{th}^{(2)}$, (■) $\nu_r^{(1)}$, (●) $\nu_r^{(3)}$ (see Sec. II).

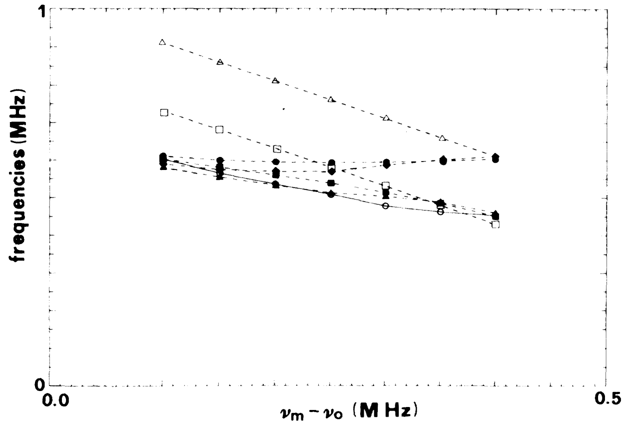

FIG. 22. Same as Fig. 21, but for $\nu_{ri}=1.29$ MHz. ▲ and ◆ correspond to $\nu_r^{(2)}$ and $\nu_r^{(4)}$, respectively.

and (2.13). The value $\nu_{\rm th}^{(1)}$ which assumes the free spectral range of the empty cavity, exhibits a good accord with the oscillation frequency, whereas $\nu_{\rm th}^{(2)}$ presents a systematic deviation. When the detuning becomes large, the agreement with $\nu_{\rm th}^{(1)}$ worsens because the numerically obtained oscillation frequency tends to become constant.

Also the Rabi frequency of the intracavity field shows a strong correlation with the oscillation frequency. There is not much difference between the results obtained using the value of the intracavity field in the unstable stationary solution and those obtained using the r.m.s. value of the intracavity field in the oscillations around the unstable state, i.e., $\nu_r^{(1)}$ is close to $\nu_r^{(2)}$, and $\nu_r^{(3)}$ is close to $\nu_r^{(4)}$. For increasing values of the detuning, when the difference between the Rabi frequency and the generalized Rabi frequency becomes significant, in the case of Fig. 21 and 22 the oscillation frequency is in better accord with the Rabi frequency. This fact is not general in our numerical analysis; however, we found more often a better agreement with the Rabi frequency rather than with the generalized Rabi frequency.

In fact, we tested the thumb rules for several choices of the parameters. Another example is given in Fig. 23, in which the oscillation frequency is graphed as a function of the pressure for $\nu_{ri}=1.44$ MHz, $\nu_m-\nu_0=\nu_p-\nu_0=240$ kHz. Note that the frequency varies very slowly with the pressure as it did in the experiment.

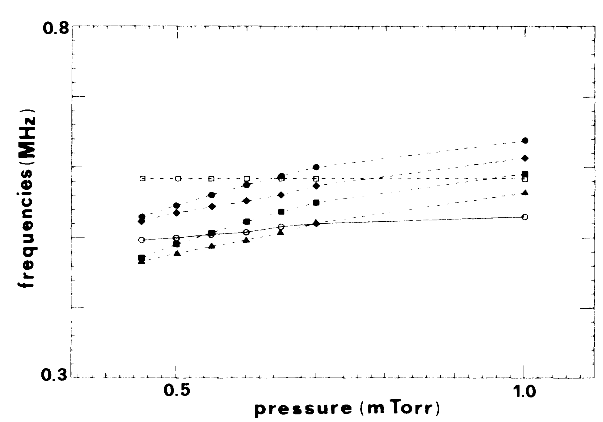

FIG. 23. The parameters not specified in Eq. (4.1) are $\nu_{ri}=1.44$ MHz, $\nu_m-\nu_0=\nu_p-\nu_0=240$ kHz. As a function of the pressure, the figure exhibits the same quantities shown in Figs. 21 and 22, with the same meaning for the symbols.

As we said, the MM instability is characterized by the fact of arising in conditions of quasiresonance between the Rabi frequency of the intracavity field and the difference $|\nu_s-\nu_0|$ between the frequency of the unstable sidemode and the input frequency. An evident confirmation is given in Fig. 24(a). Here we consider the fully resonant configuration $\nu_m=\nu_p=\nu_0$, so that the symmetrical sidemodes $\nu_{p\pm1}$ become simultaneously unstable, and the frequency $|\nu_s-\nu_0|$ is equal to the free spectral range. The input intensity is slowly swept in the backward direction and the instability arises when the Rabi frequency of the intracavity field is close to the free spectral range. Note, in this figure and in all the theoretical and experimental results of this paper, that the power-broadened linewidth is much larger than the collisional linewidth. In fact, the ratio of the two linewidths is given essentially by the parameter x defined by Eq. (2.8) which, in the case of the unstable interval of the steady-state curve shown in Fig. 24(a), is on the order of 45. In Fig. 24(b) the free spectral range is halfed with respect to the value given in Eq. (4.1). This time, we find two domains of oscillatory behavior; the one which corresponds to lower (higher) values of the input intensity arises from the instability of the modes $p\pm1$ $(p\pm2)$.

Let us now proceed to a direct comparison with the experimental results. Figure 25 is obtained by sweeping the input power forward and backward with $p=0.55$ mTorr, $\nu_m-\nu_0=\nu_p-\nu_0=317$ kHz in close correspondence to the experimental situation of Fig. 10. The similarity with

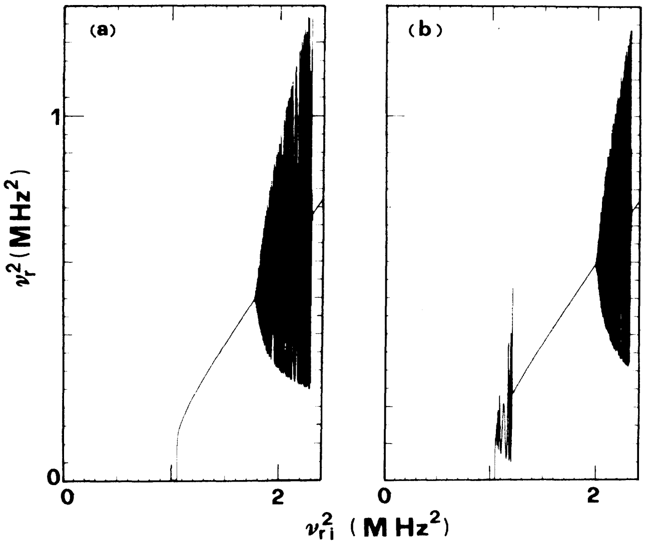

FIG. 24. (a) Parameters not specified in Eq. (4.1) are $\nu_m-\nu_0=\nu_p-\nu_0=0$, $p=0.75$ mTorr. The square of the Rabi frequency of the intracavity field, proportional to the output power, is plotted as a function of the square of the Rabi frequency of the input field, proportional to the input power, when this is slowly swept in the backward direction. (b) Same as (a), but the free spectral range of the empty cavity is now 415 kHz.

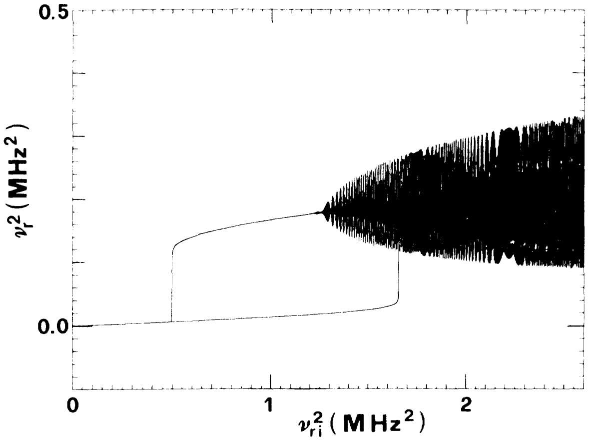

FIG. 25. Parameters not specified in Eqs. (4.1) are $\nu_m - \nu_0 = \nu_p - \nu_0 = 317$ kHz, $p = 0.55$ mTorr. The input power is slowly swept forward and backward. The square of the Rabi frequency of the intracavity field ν_r is graphed as a function of the square of the Rabi frequency of the input field ν_{ri}.

the experimental picture is remarkable; note in particular the parabolic growth of the oscillation amplitude, compare with Fig. 11(b). The oscillations are purely sinusoidal, with a frequency of approximately 465 kHz which varies by approximately 3.2% over the interval of input power shown in the figure [compare with Fig. 11(a)].

It is interesting to observe that, if the pressure is increased to a value of 0.75 mTorr, the oscillations become more complicated, as shown in Figs. 26(a) and 26(b). In the upper branch [Fig. 26 (a)] there is an interval of chaotic oscillation; the approach to chaos under variation of the input intensity occurs via breathing,[79,80] i.e., the envelope of the sinusoidal oscillations breaks itself into oscillations. The breathing pattern becomes more pronounced as the chaotic domain is approached. In the lower branch [Fig. 26(b)] there is the appearance of oscillations which were absent previously. Contrary to the pulsations in the upper branch, these lower branch oscillations have a frequency (~ 140 kHz) in substantial disagreement with the rule (2.12), even if the Rabi frequency of the intracavity field remains close to the oscillation frequency. In the experiment, neither chaotic behavior nor lower-branch oscillations have been observed.

We investigated further the case $p = 0.75$ mTorr by exploring what happens if one moves in the direction of the mean-field limit (2.10). Precisely, we decreased by a factor of 10 the parameters αl, $(1-R)$ and $\nu_p - \nu_0$ (i.e., the input frequency is shifted much closer to resonance with the mode p), leaving the remaining parameters unchanged. The lower-branch oscillations disappear, whereas the upper-branch oscillations persist and, in accord with prescriptions (2.12) and (2.13), occur beyond the bistable domain, for much larger values of the Rabi frequency of the intracavity field with respect to Fig. 26. These upper-branch oscillations are characterized by a very pronounced breathing pattern (Fig. 27).

Let us now consider the results obtained by sweeping the frequency of the input field. In correspondence to the experimental situation of Fig. 12, we fix $\nu_m = \nu_p$, $\nu_{ri} = 1.44$ MHz, and consider the three distinct values of the pressure $p = 0.9$, 0.95 and 1 mTorr. Figure 28 indicates, for each value of the detuning, the values of the input intensity (more precisely, of ν_{ri}^2) at the turning points

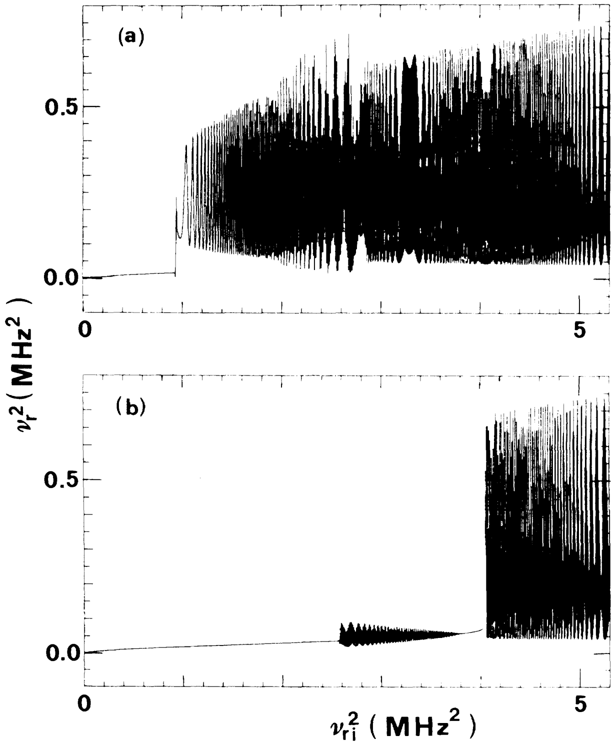

FIG. 26. Same as Fig. 25, but with $p = 0.75$ mTorr. In (a) and (b) the input intensity is swept in the backward and forward direction, respectively.

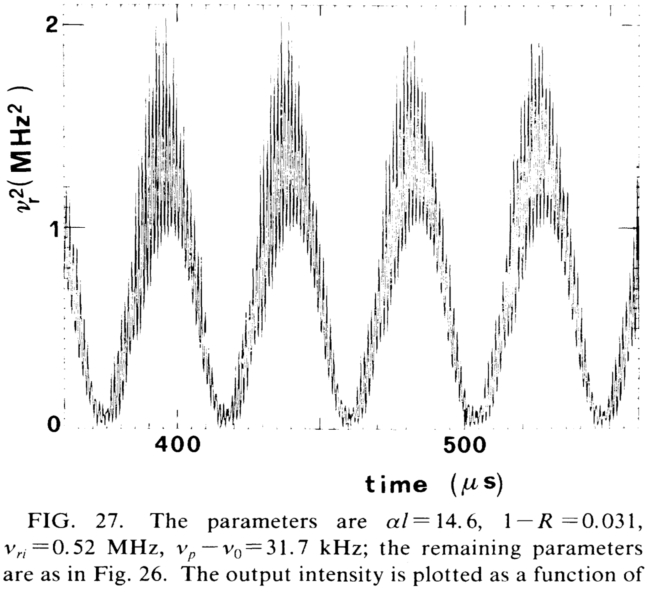

FIG. 27. The parameters are $\alpha l = 14.6$, $1-R = 0.031$, $\nu_{ri} = 0.52$ MHz, $\nu_p - \nu_0 = 31.7$ kHz; the remaining parameters are as in Fig. 26. The output intensity is plotted as a function of time in the oscillatory regime of the upper branch.

of the steady-state curve of output versus input power. There are two turning points when the steady-state curve is bistable, and four turning points when it is multistable (see, for example, Fig. 29). We note that multistability has been observed in our experiments. When the input frequency is linearly and slowly swept in the forward direction over the interval indicated in Fig. 28 for $\nu_{ri}=1.44$ MHz, in the case of Figs. 28(a) and 28(b) the system remains always in the upper branch, whereas at higher pressure [Fig. 28(c)] it precipitates to the lower branch at point *P* and comes back to the upper branch at point *Q*.

Figure 30 shows the evolution of the output intensity (more precisely of ν_r^2) under a slow linear sweep of the in-

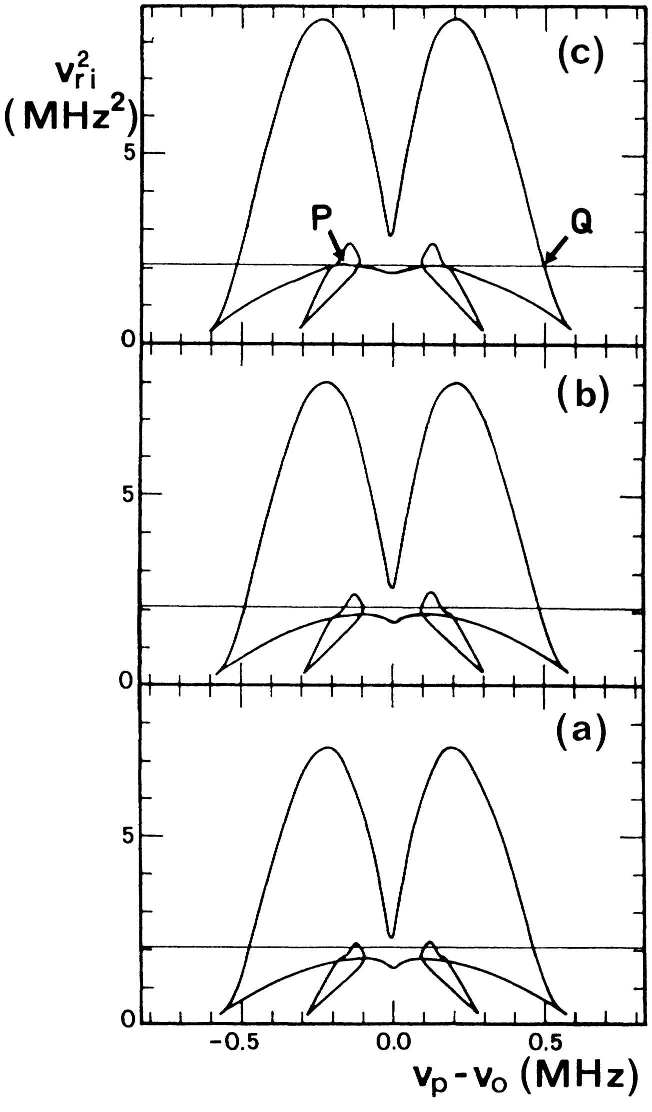

FIG. 28. The parameters not specified in Eq. (4.1) are $\nu_{ri}=1.44$ MHz, $\nu_m=\nu_p$ and (a) $p=0.9$ mTorr, (b) p=0.95 mTorr, (c) $p=1$ mTorr. The diagram shows, as a function of the detuning $\nu_p-\nu_0$, the values ν^2_{ri} which correspond to the turning points of the steady-state curve of the output power as a function of the input power. The horizontal line corresponds to the value $v^2_{ri}=(1.44)^2$ MHz^2.

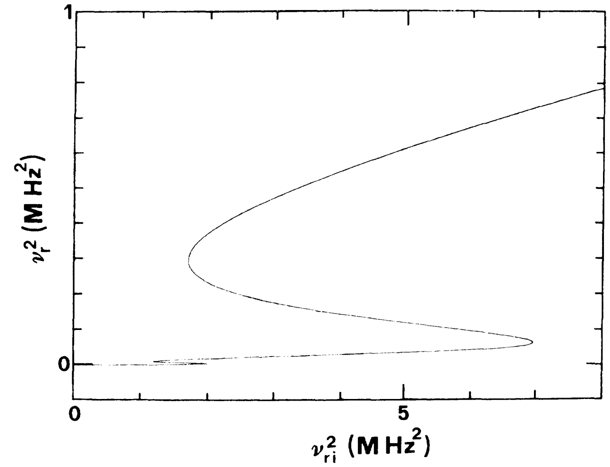

FIG. 29. Steady-state curve for $\alpha l=146$, $R=0.61$, $T=0.0043$, $p=0.9$ mTorr, $\nu_m-\nu_0=\nu_p-\nu_0=150$ kHz. The square of the Rabi frequency of the intracavity field is graphed as a function of the square of the Rabi frequency of the input field.

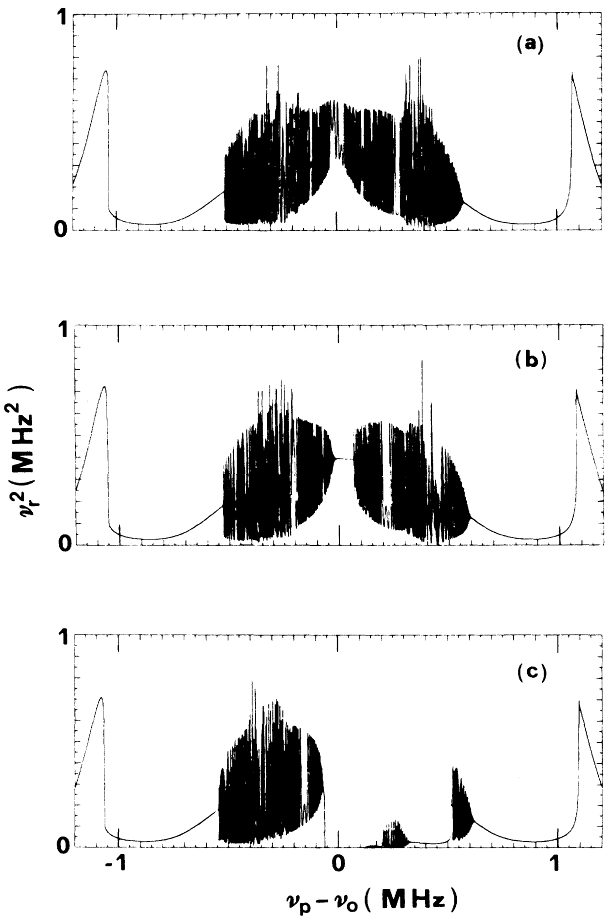

FIG. 30. The parameters are the same as in Fig. 28(a), (b), and (c), respectively. The diagrams show the behavior of ν_r^2 when the input field frequency undergoes a slow linear sweep in the forward direction.

put frequency in the forward direction. We note that the frequency distance of the two side modes from the central mode is larger than the empty-cavity free spectral range 830 kHz. The slight asymmetry in Figs. 30(a) and 30(b) arises from the nonzero velocity of the sweep, wheras the marked asymmetry in Fig. 30(c) is due to the transitions from the lower to the upper branch, and vice versa, in correspondence to points P and Q in Figs. 28(c). Figures 30(a), (b), and (c) exhibit a remarkable correlation with the corresponding experimental diagrams Figs. 12(b), (c), and (d), respectively. They show also some significant differences.

(i) In the numerical simulations, the unstable regions are much more extended and the oscillation amplitude is much larger.

(ii) The experiment never showed self-oscillations when the cavity, the molecules, and the input field are exactly on resonance, contrary to what occurs, for example, in Figs. 24 and 30(a).

(iii) The numerical results exhibit lower-branch oscillations as in Figs. 26(b) and 30(c).

These features, and more in general, the reduced effects of the instability in the experiment in comparison with the computer simulations, can be ascribed to the fact that the theory is formulated for a ring cavity and a homogeneously broadened molecular system, and assumes the plane-wave approximation. The experiment, on the other hand, uses a Fabry-Pérot cavity, in which the electric field displays not only a longitudinal standing-wave configuration, but also a definite radial variation; furthermore, the molecular system is strictly speaking inhomogeneously broadened, even if the power-broadened homogeneous linewidth is much larger than the inhomogeneous linewidth.

It is well known that a Gaussian radial variation of the electric field destroys the MM instability in the resonant condition $\nu_m = \nu_p = \nu_0$,[81] whereas the instability persists in detuned configurations.[17,82] The analysis of the single-mode instability shows that the Gaussian averaging washes out period doubling and chaotic behavior.[31] The instability is reduced also by the standing-wave longitudinal variation of the electric field in the Fabry-Pérot cavity.[83] Finally, the inhomogeneous broadening decreases the side-mode gain[18] and therefore also reduces the unstable domains.

Figure 31 considers the antiresonant configuration in which the molecular line is set halfway between modes $p-1$ and p; as in Fig. 30, the input frequency is linearly swept in the forward direction. Again, the unstable domains are much wider than in the experiment (see Fig. 13). Furthermore, the oscillations are chaotic almost everywhere. In the narrow domains of sinusoidal oscillations in the frequency interval shown in Fig. 31; the frequency is approximately equal to 290 kHz, in reasonable accord with the Rabi frequency $\nu_r^{(1)}$ and $\nu_r^{(2)}$. In the application of the rule (2.12), it is not obvious whether ν_s must be identified with ν_{p-1} or with ν_{p+1}; the choice of $\nu_s = \nu_{p-1}$ for $\nu_m - \nu_0 = 100$ kHz gives a reasonable agreement with Eq. (2.12), whereas for $\nu_m - \nu_0 = 300$ kHz Eq. (2.12) disagrees from the numerical oscillation frequency for neither choice $\nu_s = \nu_{p\pm1}$.

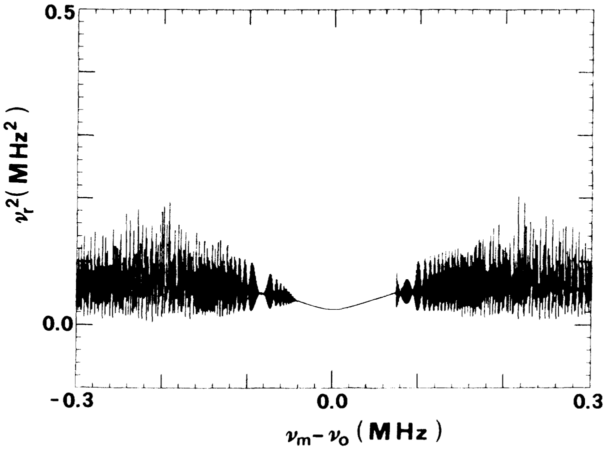

FIG. 31. Same as Fig. 30, but for $p = 0.6$ mTorr, $\nu_{ri} = 1.9$ MHz, $\nu_p - \nu_m = 415$ kHz.

Finally, in Fig. 32 we consider a case in which the steady-state curve of output versus input power exhibits a small domain of multistability, similar to Fig. 29. Let us focus on the small hysteresis cycle in the multistable domain; in the upper branch of this cycle we found self-oscillations with a period-doubling route to chaos which is illustrated in Fig. 32. It is possible that the oscillations we discovered in the lower branch, and in the multistable domain in the lower branch, represent a bridge between the Bonifacio-Lugiato instability,[6] which arises in the upper branch from the coherent exchange of energy between field and atoms (Rabi frequency) and the Ikeda instability,[10] which arises also in the lower branch under incoherent conditions.

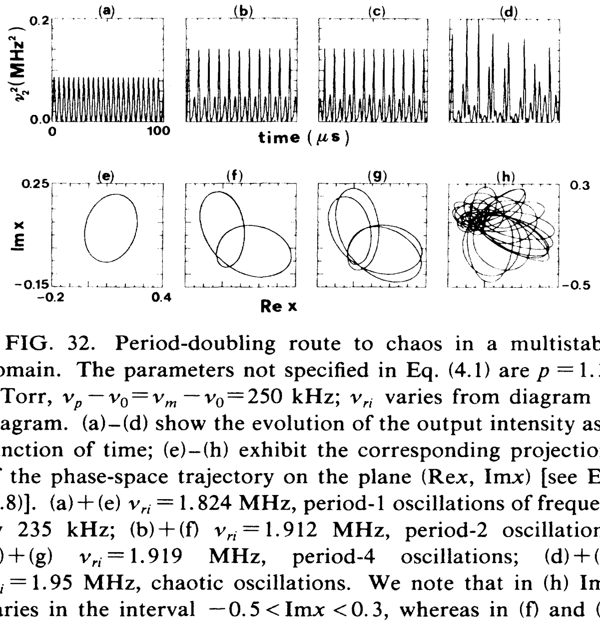

FIG. 32. Period-doubling route to chaos in a multistable domain. The parameters not specified in Eq. (4.1) are $p = 1.35$ mTorr, $\nu_p - \nu_0 = \nu_m - \nu_0 = 250$ kHz; ν_{ri} varies from diagram to diagram. (a)–(d) show the evolution of the output intensity as a function of time; (e)–(h) exhibit the corresponding projections of the phase-space trajectory on the plane (Rex, Imx) [see Eq. (2.8)]. (a)+(e) $\nu_{ri} = 1.824$ MHz, period-1 oscillations of frequency 235 kHz; (b)+(f) $\nu_{ri} = 1.912$ MHz, period-2 oscillations; (c)+(g) $\nu_{ri} = 1.919$ MHz, period-4 oscillations; (d)+(h) $\nu_{ri} = 1.95$ MHz, chaotic oscillations. We note that in (h) Imx varies in the interval $-0.5 < \mathrm{Im}x < 0.3$, whereas in (f) and (g) the interval of variation of Imx is the same as in (e).

Noted added in proof. In very recent experiments, a sine-wave self-pulsing at a frequency of about 1.5 MHz has been evidenced and attributed to the destabilization of the second side mode. This result, which complements those analyzed in this paper, will be presented in a forthcoming brief report.

ACKNOWLEDGMENTS

We are deeply indebted to Professor D. K. Bandy and Professor L. M. Narducci for providing us the numerical code to solve the Maxwell-Bloch equations. Thanks are also due to Professor E. Arimondo who prompted us to undertake the experimental study, to Dr. J. Zemmouri for his assistance in the first experiments, to Professor N. B. Abraham for suggesting the measurement of the heterodyne spectrum, and to Professor H. M. Gibbs for a stimulating discussion. The circular waveguide components used have been kindly donated by the Centre National d'Etude des Télécommunications through Dr. A. Boulouard. This work was carried out in the framework of the European Economic Community twinning project on "Dynamics of Nonlinear Optical Systems." Laboratoire de Spectroscopie Hertzienne de l'Université de Lille is Unité associée au Centre National de la Recherche Scientifique and is also supported by the Région Nord–Pas-de-Calais.

---

[1] A. Z. Grazyuk and A. N. Oraevski, Radiotekh. Elektron. **9**, 524 (1964) [Radio. Eng. Electron. Phys. (USSR) **9**, 424 (1964)].

[2] H. Haken, Z. Phys. **190**, 327 (1966).

[3] H. Risken, C. Schmid, and W. Weidlich, Z. Phys. **194**, 337 (1966).

[4] H. Risken and K. Nummedal, J. Appl. Phys. **39**, 4662 (1968).

[5] R. Graham and H. Haken, Z. Phys. **213**, 420 (1968).

[6] R. Bonifacio and L. A. Lugiato, Lett. Nuovo Cimento **21**, 505 (1978); **21**, 510 (1978).

[7] S. L. McCall, Appl. Phys. Lett. **32**, 284 (1978).

[8] L. W. Casperson, IEEE J. Quantum. Electron. **QE-14**, 756 (1978).

[9] H. Haken, Phys. Lett. **53A**, 77 (1975).

[10] K. Ikeda, Opt. Commun. **30**, 257 (1979).

[11] J. Opt. Soc. Am. B **2**, feature issue (1985).

[12] *Optical Instabilities,* edited by R. W. Boyd, M. G. Raymer, and L. M. Narducci (Cambridge University Press, Cambridge, England, 1986).

[13] *Instabilities and Chaos in Quantum Optics,* edited by F. T. Arecchi and R. Harrison (Springer-Verlag, Berlin, 1987).

[14] J. Opt. Soc. Am. B, feature issue (May, 1988).

[15] *Instabilities and Chaos in Quantum Optics II,* edited by N. B. Abraham, F. T. Arecchi, and L. A. Lugiato (Plenum, New York, 1988).

[16] H. M. Gibbs, F. A. Hopf, D. L. Kaplan, and R. L. Shoemaker, Phys. Rev. Lett. **46**, 474 (1981).

[17] L. A. Lugiato and L. M. Narducci, Phys. Rev. A **32**, 1576 (1985).

[18] S. L. McCall, Phys. Rev. A **9**, 1515 (1974).

[19] L. W. Casperson, Phys. Rev. A **21**, 911 (1980).

[20] S. T. Hendow and M. Sargent III, Opt. Commun. **40**, 385 (1982).

[21] L. W. Hillman, R. W. Boyd, and C. R. Stroud, Jr., Opt. Lett. **7**, 426 (1982).

[22] Y. Silberberg and I. Bar-Joseph, Opt. Commun. **48**, 53 (1983).

[23] W. J. Firth, E. M. Wright, and E. Cummins, in *Optical Bistability 2,* edited by C. R. Bowden, H. M. Gibbs, and S. L. McCall (Plenum, New York, 1984), p. 111.

[24] B. R. Mollow, Phys. Rev. A **5**, 2217 (1972).

[25] A. M. Bonch-Bruevich, V. A. Khodovoi, and N. A. Chigir, Zh. Eksp. Teor. Fiz. **67**, 2069 (1974) [Sov. Phys.—JETP **40**, 1027 (1975)].

[26] F. Y. Wu, S. Ezekiel, M. Ducloy, and B. R. Mollow, Phys. Rev. Lett. **38**, 1077 (1977).

[27] L. A. Lugiato, L. M. Narducci, D. K. Bandy, and C. A. Pennise, Opt. Commun. **43**, 281 (1982); L. A. Lugiato and L. M. Narducci, in *Coherence and Quantum Optics V,* edited by L. Mandel and E. Wolf (Plenum, New York, 1984), p. 941. A related instability in a Kerr medium was discovered by K. Ikeda and O. Akimoto, Phys. Rev. Lett. **48**, 617 (1982).

[28] L. A. Lugiato, R. J. Horowicz, G. Strini, and L. M. Narducci, Phys. Rev. A **30**, 1366 (1984).

[29] L. A. Orozco, A. T. Rosenberger, and H. J. Kimble, Phys. Rev. Lett. **53**, 2547 (1984).

[30] L. A. Orozco, M. G. Raizen, A. T. Rosenberger, and H. J. Kimble, in *Optical Bistability III,* edited by H. M. Gibbs, P. Mandel, N. Peyghambarian, and S. D. Smith (Springer-Verlag, Berlin, 1986), p. 307

[31] H. J. Kimble, L. A. Orozco, A. T. Rosenberger, L. A. Lugiato, M. L. Asquini, M. Brambilla, and L. M. Narducci (unpublished).

[32] L. A. Lugiato, Opt. Commun. **33**, 108 (1980).

[33] R. Bonifacio, M. Gronchi, and L. A. Lugiato, Opt. Commun. **30**, 129 (1979).

[34] M. Gronchi, V. Benza, L. A. Lugiato, P. Meystre, and M. Sargent III, Phys. Rev. A **24**, 1419 (1981).

[35] L. A. Lugiato, V. Benza, L. M. Narducci, and J. D. Farina, Z. Phys. B **49**, 351 (1983).

[36] B. Ségard and B. Macke, Phys. Rev. Lett. **60**, 412 (1988).

[37] B. Ségard and B. Macke, in *Optical Bistability IV,* edited by W. Firth, N. Peyghambarian, and A. Taller [reprinted in J. Phys. (Paris) **49**, C2-371 (1988) (Supplement No. 6)].

[38] L. W. Hillman, J. Krasinski, R. W. Boyd, and C. R. Stroud, Jr. Phys. Rev. Lett. **52**, 1605 (1984).

[39] E. H. Hogenboom, W. Klische, C. O. Weiss, and A. Godone, Phys. Rev. Lett. **55**, 2571 (1985).

[40] C. O. Weiss and J. Brock, Phys. Rev. Lett. **57**, 2804 (1986).

[41] L. A. Lugiato, C. Oldano, Wang Kaige, L. Santirana, L. M. Narducci, F. Prati, and M. Brambilla, in Ref. 37, p. 343.

[42] L. A. Lugiato, in *Progress in Optics,* edited by E. Wolf (North-Holland, Amsterdam, 1984), Vol. XXI, p. 69.

[43] L. A. Lugiato, L. M. Narducci, and M. F. Squicciarini, Phys. Rev. A **34**, 3101 (1986).

[44] J. C. Englund, R. R. Snapp, and W. C. Schieve, in *Progress in Optics,* edited by E. Wolf (North-Holland, Amsterdam, 1984), Vol. XXI, p 335.

[45] R. W. Boyd, M. G. Raymer, P. Narum, and D. J. Harter,

Phys. Rev. A **24**, 411 (1981).

[46] D. Grandclément, G. Grynberg, and M. Pinard, Phys. Rev. Lett. **59**, 40, 44 (1987).

[47] G. Khitrova, J. F. Valley, and H. M. Gibbs, Phys. Rev. Lett. **60**, 1126 (1988).

[48] S. Haroche and F. Hartman, Phys. Rev. A **6**, 1280 (1972).

[49] M. L. Asquini, L. A. Lugiato, H. J. Carmichael, and L. M. Narducci, Phys. Rev. A **33**, 360 (1986).

[50] W. Gordy and R. L. Cook, *Microwave Molecular Spectra* (Wiley, New York, 1984), p. 117.

[51] F. C. De Lucia and W. Gordy, Phys. Rev. **187**, 58 (1969).

[52] Taking account of the difference between the g factors of ^{15}N and ^{14}N and between the rotational constants of $HC^{15}N$ and $HC^{14}N$, these parameters have been derived from those of $HC^{14}N$ given by F. J. Lovas, J. Phys. Chem. Ref. Data **7**, 1750 (1978).

[53] E. F. Pearson, R. A. Creswell, M. Winnewisser, and G. Winnewisser, Z. Naturforsch. **31**, 1394 (1976).

[54] L. Allen and J. H. Eberly, *Optical Resonance and Two-level Atoms* (Wiley, New York, 1975).

[55] W. L. Ebenstein and J. S. Muenter, J. Chem. Phys. **80**, 3989 (1984).

[56] B. Senitzky, G. Gould, and S. Cutler, Phys. Rev. **130**, 1460 (1963).

[57] M. Colmont, J. Mol. Spectrosc. **114**, 298 (1985).

[58] See Ref. 50, pp. 48 and 49.

[59] B. H. Armstrong, J. Quant. Spectrosc. Rad. Transfer **7**, 61 (1967).

[60] B. Ségard, J. Zemmouri, and B. Macke, Opt. Commun. **63**, 339 (1987); J. Zemmouri, thesis, Université de Lille, France, 1987.

[61] B. Ségard, J. Zemmouri, and B. Macke, Europhys. Lett. **4**, 47 (1987).

[62] *International Conference on Millimetric Waveguide Systems, London, 1976* (IEE, London, 1976); see also the special issue of the Bell Syst. Tech. J. **56**, (10), 1977.

[63] J. Billard, Nouv. Rev. Opt. **7**, 315 (1976); C. R. Acad. Sci. Paris B **286**, 247 (1978).

[64] J. Durnin, J. J. Micelli, and J. H. Eberly, Phys. Rev. Lett. **58**, 1499 (1987); J. Durnin, J. Opt. Soc. Am A **4**, 651 (1987).

[65] M. Born and E. Wolf, *Principles of Optics* (Pergamon, Oxford, 1975).

[66] This ratio is maximum (1.31) for $R_0=0.62$ but the corresponding finesse is poor (3.8). In fact, the best compromise is achieved when the product $F \times E_c^0$ is maximum, that is for $R_0=0.89$, leading to $F=7.1$ and $E_c^0/E_i=0.85$, values not far from those attained for $R_0=0.95$, which slightly favors the finesse at the expense of the intracavity field.

[67] A. C. Legon, D. J. Millen, and S. C. Rogers, Proc. R. Soc. London, Ser. A **370**, 213 (1980).

[68] The calibration of the gauge with HCN was not made in Refs. 36, 60, and 61. The pressures given in these papers have then to be multiplied by 0.7 whereas T_2 and $\alpha_\infty l$ (see Ref. 61) have to be divided by this quantity.

[69] E. A. J. Marcatili, in *Proceedings of the Symposium on Quasioptics, New York, 1964,* edited by J. Fox (Polytechnic, Brooklyn, 1964), pp. 535–542.

[70] J. H. King and J. L. Wong, IEEE Trans. Microw. Theo. Techn. MTT **19**, 116 (1971).

[71] A. Boulouard, Technical report, CNET (1977) (available from CNET-B, 22301 Lannion Cedex, France). See also Ref. 70 and R. P. Hecken and A. Anuff, IEEE Trans. Microwave Theory Tech. **21**, 374 (1973).

[72] In some cases, a second bistability appears both on the observed and computed curves (multistability). The corresponding output levels are very low.

[73] $\nu_{ri}=1.33$ MHz corresponds to $E_i \cong 1.52$ V/cm and to a power density approximately equal to 3.1 mW/cm^2. In a plane-wave model, the power through an area equal to the waveguide cross section is then equal to about 87 mW.

[74] See, e.g., J. M. T. Thompson and H. B. Stewart, *Nonlinear Dynamics and Chaos* (Wiley, Chichester, 1986), pp. 115–117.

[75] E. Arimondo, A. Gozzini, L. Lovitch, and E. Pistelli, in *Optical Bistability,* edited by C. M. Bowden, M. Ciftan, and H. R. Robl (Plenum, New York, 1981), p. 151.

[76] W. J. Sandle and A. Gallagher, Phys. Rev. A **24**, 2017 (1981).

[77] Note that for $\nu_m - \nu_0 < 0$ the relevant side mode would be the mode $(p+1)$.

[78] L. A. Lugiato, L. M. Narducci, E. V. Eschenazi, D. K. Bandy, and N. B. Abraham, Phys. Rev. A **32**, 1563 (1985).

[79] M. Mayr, H. Risken, and D. Vallmer, Opt. Commun. **36**, 480 (1981).

[80] L. A. Lugiato and M. Milani, Z. J. Phys. B **50**, 171 (1983).

[81] L. A. Lugiato, L. M. Narducci, D. K. Bandy, and C. A. Pennise, Opt. Commun. **46**, 64 (1983).

[82] L. A. Lugiato and M. Milani, J. Opt. Soc. Am. B **2**, 15 (1985).

[83] M. Sargent III, Kvant. Elektron. (Moscow) **7**, 2151 (1980) [Sov. J. Quant. Electron, **10**, 1247 (1980)]; F. Casagrande, L. A. Lugiato, and M. L. Asquini, Opt. Commun. **32**, 492 (1980).